# Supporting Information

## Mechanism of fully-reversible, pH-sensitive inhibition of human glutamine synthetase by tyrosine nitration

Benedikt Frieg[1,2], Boris Görg[3], Natalia Qvartskhava[3], Thomas Jeitner[4], Nadine Homeyer[1], Dieter Häussinger[3*] and Holger Gohlke[1,2*]

[1] Institute for Pharmaceutical and Medicinal Chemistry, Heinrich Heine University Düsseldorf, Düsseldorf, Germany

[2] John von Neumann Institute for Computing (NIC), Jülich Supercomputing Centre (JSC), and Institute of Biological Information Processing (IBI-7: Structural Biochemistry), Forschungszentrum Jülich GmbH, Jülich, Germany

[3] Clinic for Gastroenterology, Hepatology, and Infectious Diseases, Heinrich Heine University Düsseldorf, Düsseldorf, Germany

[4] Department of Biochemistry and Molecular Biology, New York Medical College, Valhalla, NY, USA

[*]Corresponding authors: (H.G.) Universitätsstr. 1, 40225 Düsseldorf, Germany, Phone: (+49) 211 81 13662, Fax: (+49) 211 81 13847, E-mail: gohlke@uni-duesseldorf.de or h.gohlke@fz-juelich.de; (D.H.) Moorenstr. 5, 40225 Düsseldorf, Phone : (+49) 211 81 16330, Fax : (+49) 211 81 18752, E-mail : haeussin@uni-duesseldorf.de

## Table of Contents

## Supporting Figures

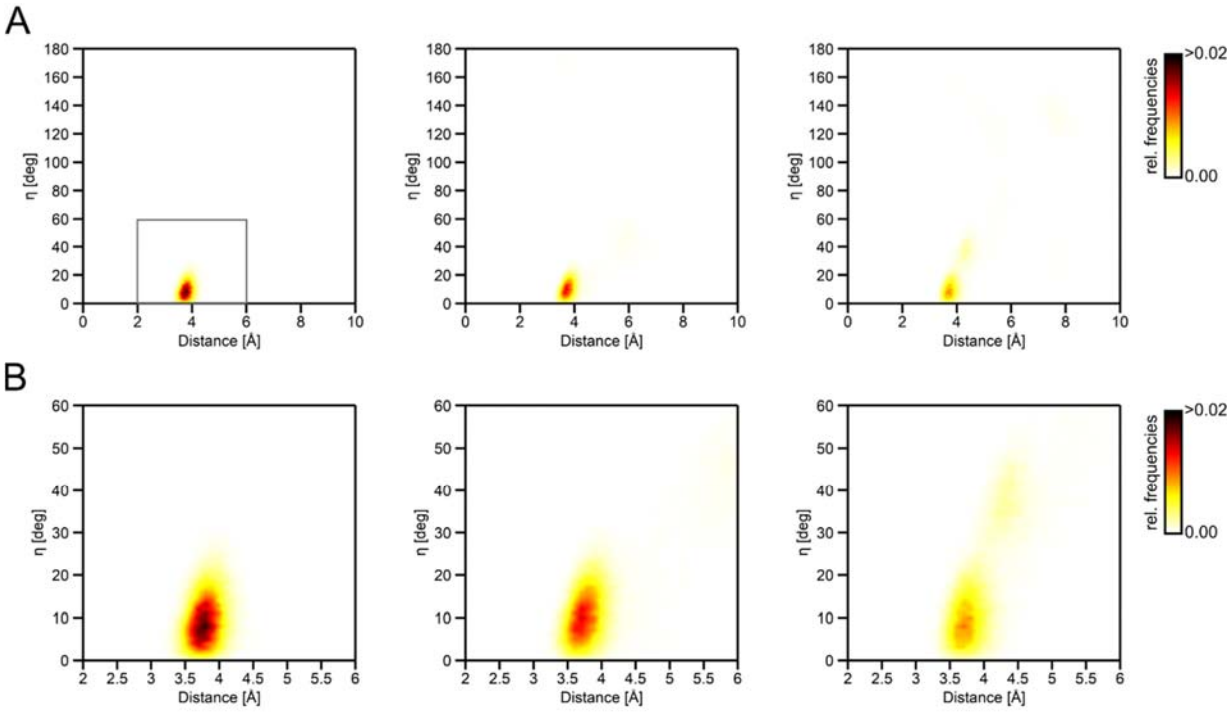


**Figure S1: Conformational analysis of ATP stacking.**
**A**, **B**: 2D histograms (normalized by the sum over all bins) of the distance between the centers of mass of the phenyl ring (residue Y336 and nitro variants) and the purine ring system (ATP) (bin size 0.1 Å) and the angle η between the ring planes of the phenyl ring (residue Y336/TYN336/TYD336) and the purine ring system (ATP) (bin size 1°). The gray box in the upper left panel depicts the area considered for the close-up view in **B**. From left to right the plots show the results for wild type GS, $GS_{TYN}$, and $GS_{TYD}$.

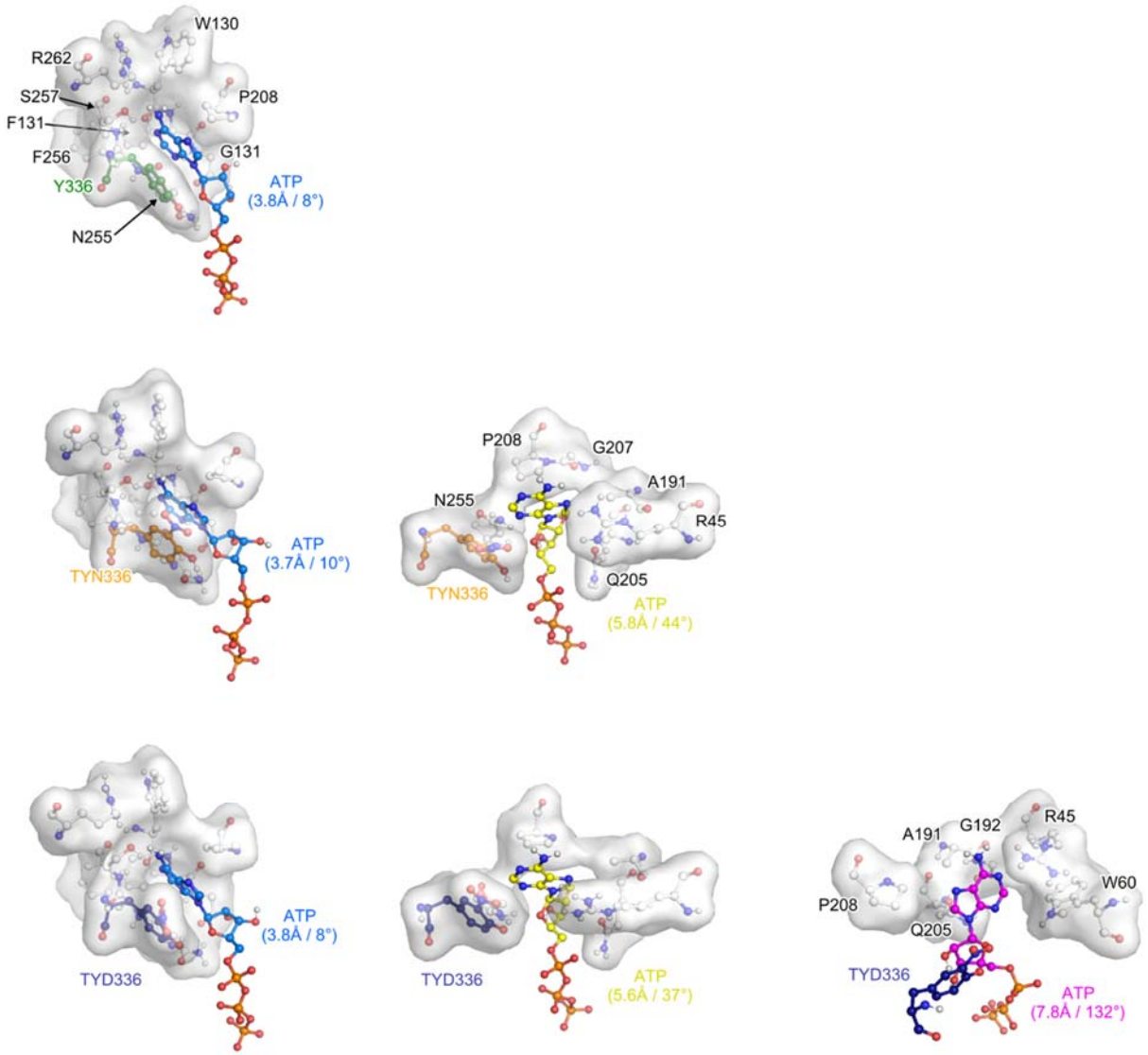


**Figure S2: Binding poses of ATP during molecular dynamics simulations.**
Close-up view of per-residue interactions of representative ATP poses extracted from the MD trajectory for wild type GS (top), $GS_{TYN}$ (middle), and $GS_{TYD}$ (bottom). Representative ATP configurations belonging to the main populations in Figure 2A and B in the main text (labels depicting "distance [Å]/η [°]" combinations) are shown as opaque ball-stick models. The general color scheme matches Figure 2C. Residues that bind to the purine ring in ATP have at least one atom within 4 Å around ATP's adenine moiety and are shown as a white ball-stick models with a transparent surface. The black labels depict the residue numbers following the numbering in ref.[1].

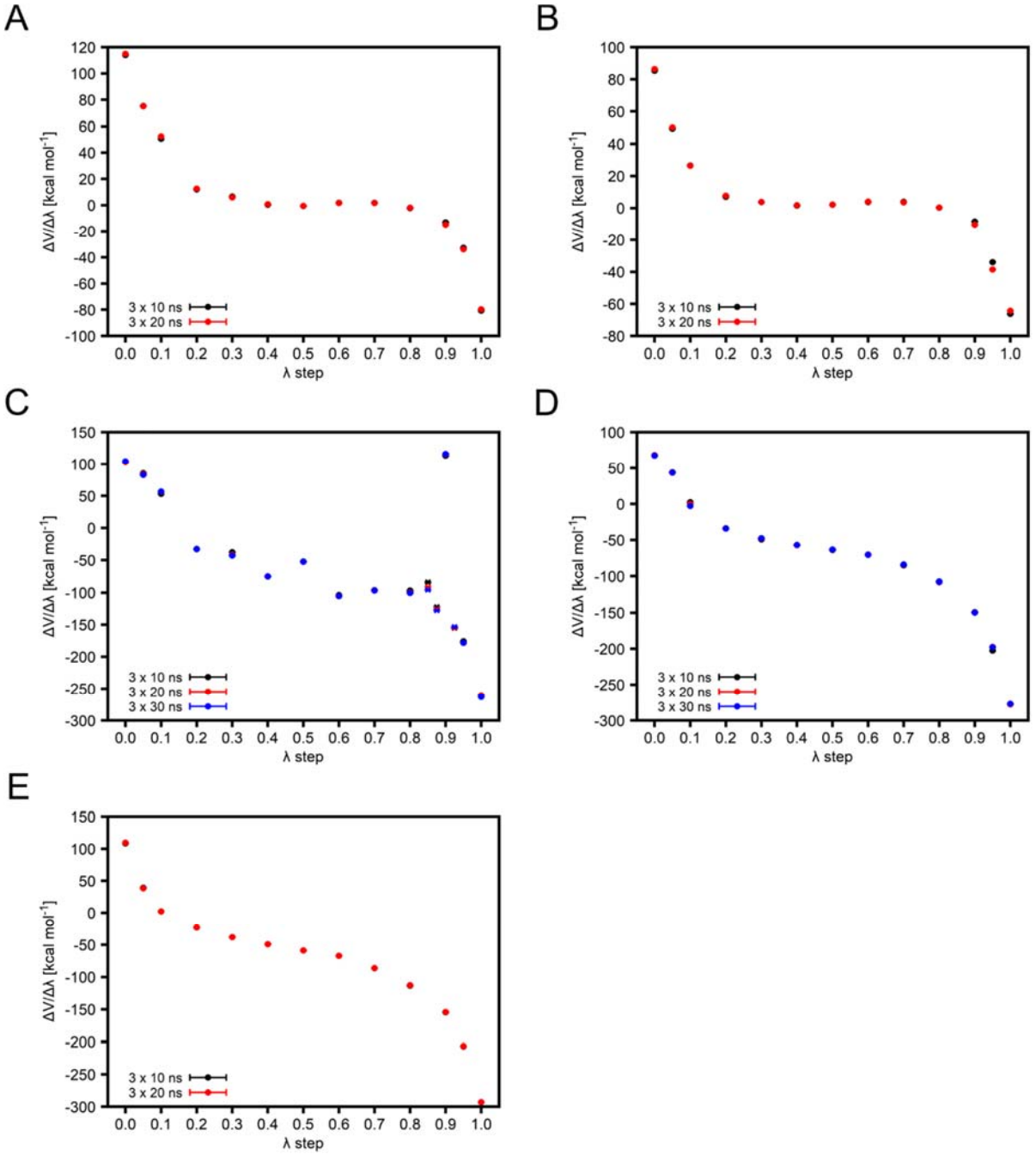


**Figure S3: Results from thermodynamic integration calculations.**
Average dV/dλ values after 3 × 10 ns (black), 3 × 20 ns (red), and 3 × 30 ns (blue) of transformation simulations of TYN336 into Y336 in $GS_{ATP}$ state (**A**), TYN336 (λ = 0.00) into Y336 (λ = 1.00) in $GS_{Apo}$ state (**B**), TYN336 (λ = 0.00) into TYD336 (λ = 1.00) in $GS_{ATP}$ state (**C**), TYN336 (λ = 0.00) into TYD336 (λ = 1.00) in $GS_{Apo}$ state (**D**), and ACE-TYN-NME (λ = 1.00) into ACE-TYD-NME (λ = 1.00) in the model systems (**E**). Transformation simulations were performed at λ = 0.00, 0.05, 0.10, 0.20, …, 0.90, 0.95, 1.00. In **C** (TYN336 (λ = 0.00) into TYD336 (λ = 1.00)), additional simulations were performed at λ = 0.85, 0.875, 0,925 and average dV/dλ are plotted with an × . Error bars denote the standard error of the mean (SEM), which is always ≤ 0.01 kcal $mol^{-1}$ at the end of transformation simulation.

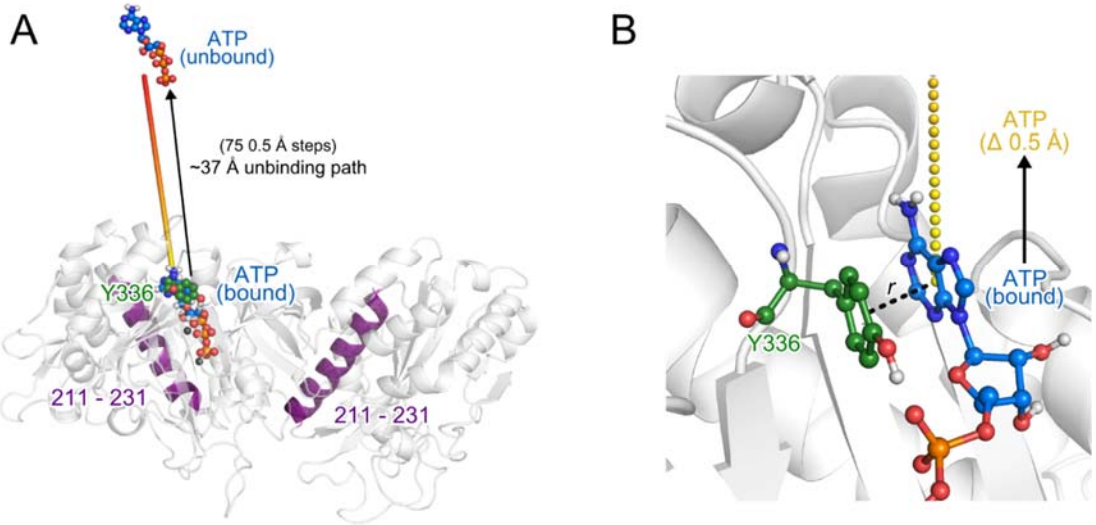


**Figure S4: Setup of the potential of mean force calculations.**
**A:** $GS_{ATP}$ dimer (white cartoon) as used for umbrella sampling. ATP (blue) was placed along a ~37 Å unbinding path determined by random acceleration molecular dynamics[2]. Each center of mass (COM) of the purine ring is depicted as spheres colored yellow-orange-red. Residues 211 – 231 (purple) of both subunits are fixed with positional restraints of 0.5 kcal $mol^{-1}$ $Å^{-2}$ during simulations to ensure the correct relative orientation of the protein. **B**: Close-up view of the ATP binding site. ATP (blue) and Y336 (green) form stacking interactions in the bound state. For umbrella sampling, the ATP molecule was initially placed in 0.5 Å intervals (ATP, red) along the unbinding path (schematically depicted by COM spheres of the purine ring system and an arrow). The reaction coordinate *r* for umbrella sampling simulations is defined as the distance between the centers of mass of Y336's benzene ring and ATP's purine ring system.

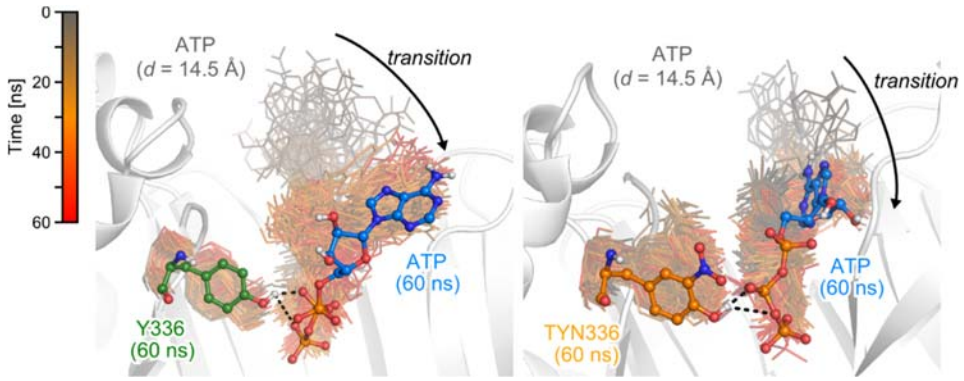


**Figure S5: Time traces of ATP and residue 336 during umbrella sampling simulations.**
Time traces during umbrella sampling simulations for wild type glutamine synthetase (GS) (left) and $GS_{TYN}$ (right) that were restrained to $d$ = 14.5 Å (colored according to the color ranges on the left). An arrow depicts the major motion of ATP.

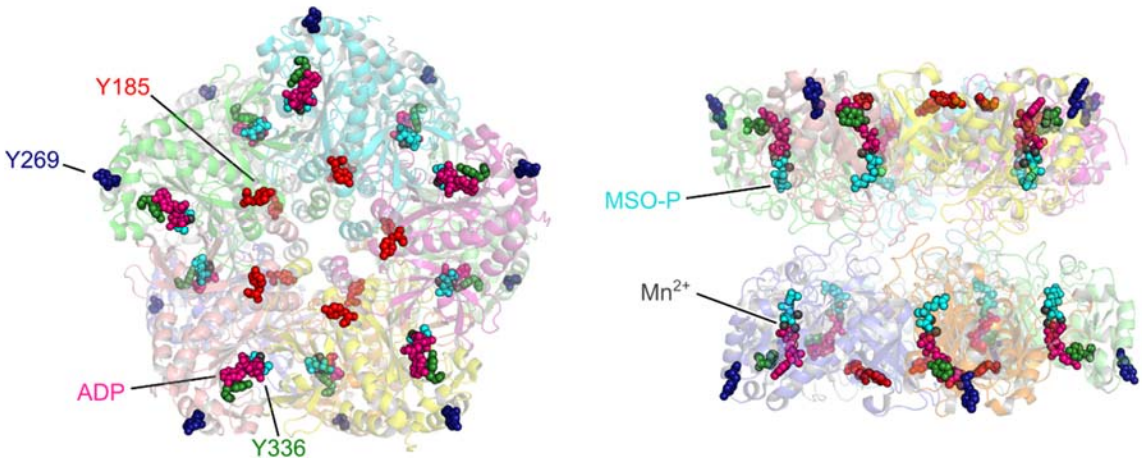


**Figure S6: Potential nitration sites in human glutamine synthetase.**
The X-ray structure in top view (left panel) and side view (right panel) of human glutamine synthetase (PDB-ID 2QC8[1]) shown as cartoon. The individual subunits are colored differently. The potential nitration sites Y185, Y269[3], and Y336[4-5] are shown as red, blue, and green sphere-model. Structurally bound ADP (magenta), L-methionine-*S*-sulfoximine phosphate (MSO-P, cyan), and manganese ions ($Mn^{2+}$, grey) are also shown as spheres and depict the location of the catalytic sites.

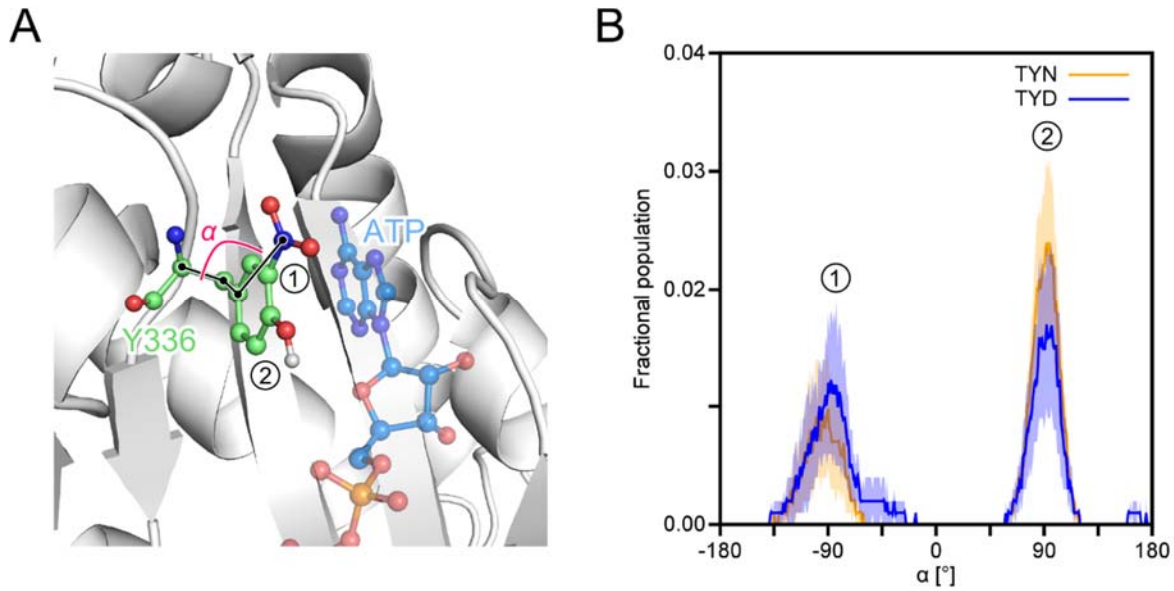


**Figure S7: Conformational analyses of Y336.**
**A**: Close-up view of nitrated Y336 (green, ball-stick model) within $GS_{TYN}$. ATP (blue, ball-stick model) was not present during molecular dynamics simulations in the $GS_{Apo}$ state but was added for visualization purposes. The dihedral $\alpha$ was used to measure the orientation of the nitro group within the ATP binding site; two orientations (① and ②) are primarily populated (see panel **B**). **B:** Mean fractional populations (normalized by the sum of all bins) with the standard error of the mean (SEM; depicted as filled curve) of $\alpha$ (bin size 0.1 Å); $GS_{TYN}$: orange; $GS_{TYD}$: blue. Labels ① and ② refer to the orientations of the nitro group shown in panel A.

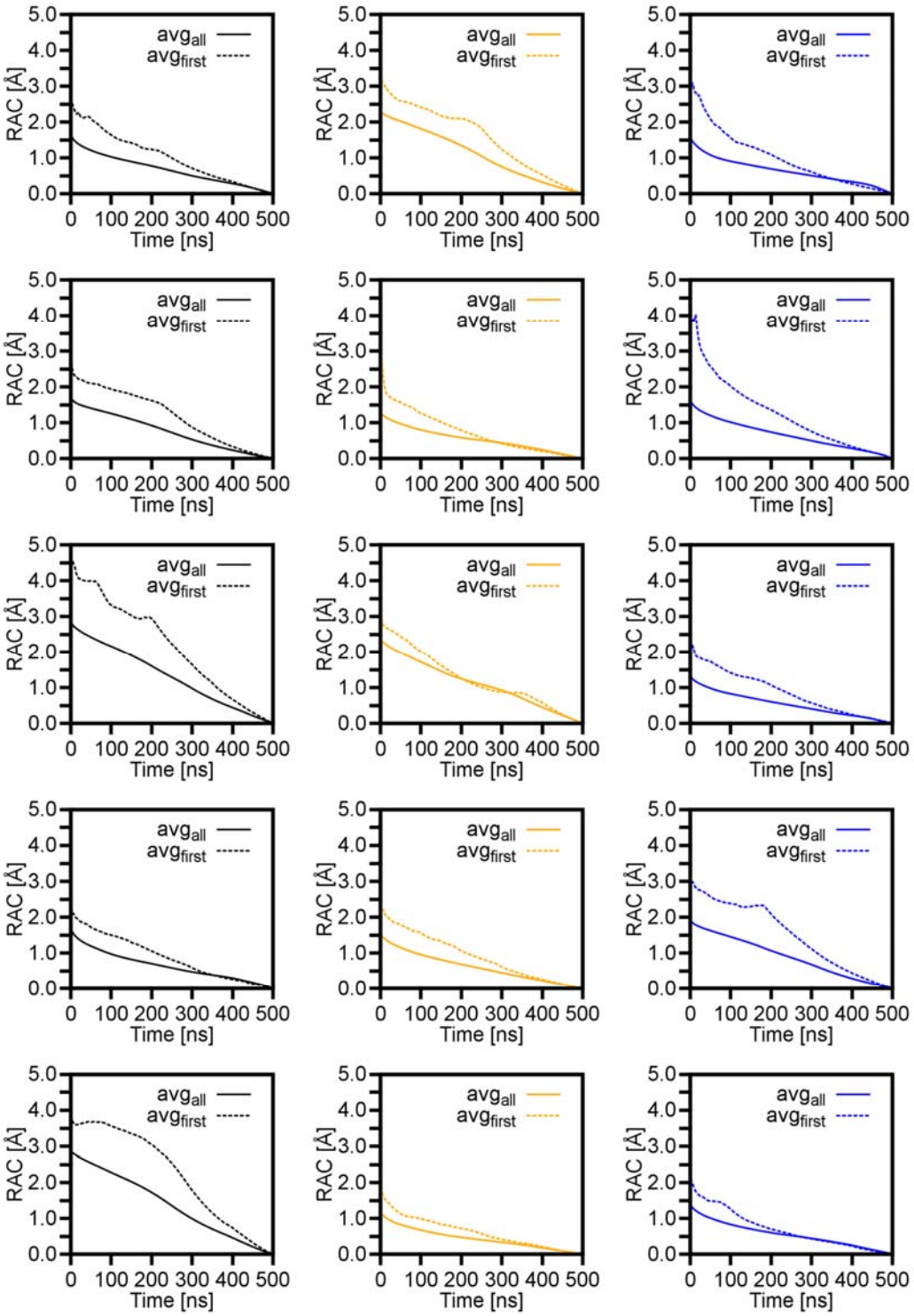


**Figure S8: RMS average correlation function for all backbone atoms.**
RMS average correlation (RAC) computed for all backbone atoms of the $GS_{ATP}$ structure of wild type glutamine synthetase (GS) (black), $GS_{TYN}$ (orange), and $GS_{TYD}$ (blue) for five molecular dynamics trajectories each. The RMS fit was either performed to the overall average structure (solid) or the first calculated running average structure, where the averaging occurs from zero to the depicted time (dotted).

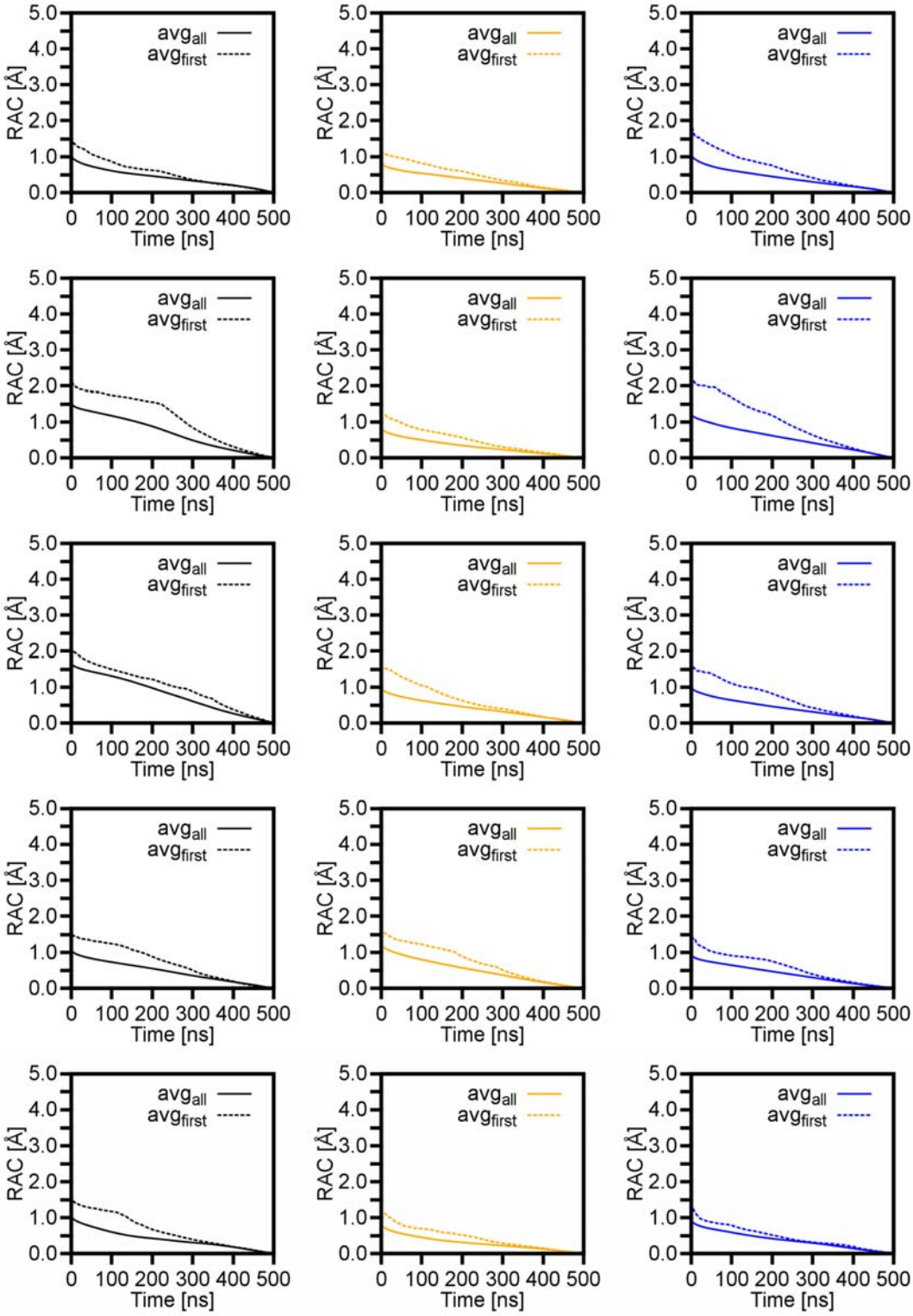


**Figure S9: RMS average correlation function for $GS_{core}$ backbone atoms.**
RMS average correlation (RAC) computed for $GS_{core}$ backbone atoms of the $GS_{ATP}$ structure of wild type glutamine synthetase (GS) (black), $GS_{TYN}$ (orange), and $GS_{TYD}$ (blue) for five molecular dynamics trajectories each. The RMS fit was either performed to the overall average structure (solid) or the first calculated running average structure, where the averaging occurs from zero to the depicted time (dotted).

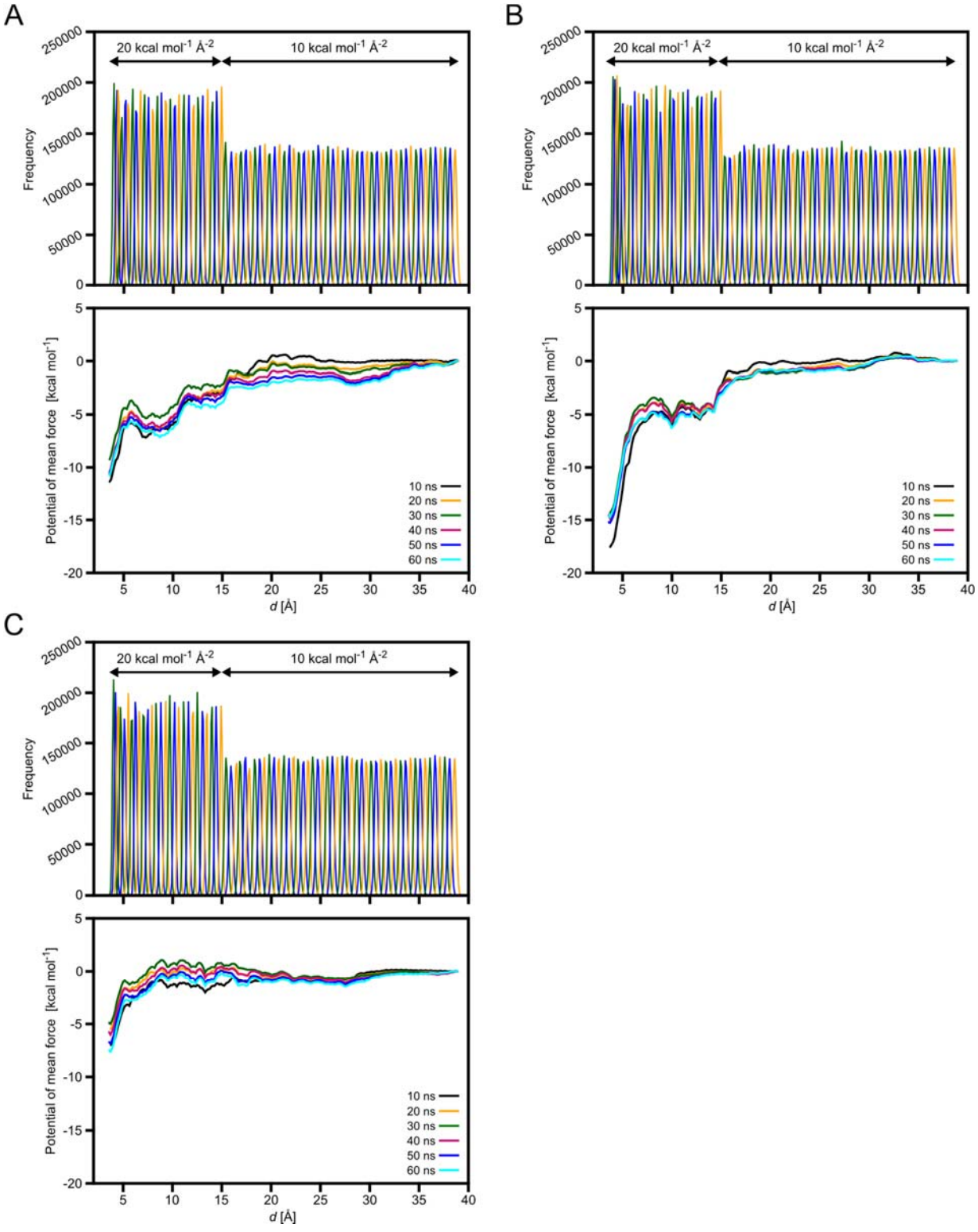


**Figure S10: Umbrella sampling and potentials of mean force for ATP binding to glutamine synthetase (GS) variants.**
Frequencies of sampled reaction coordinates during umbrella sampling simulations (top) and derived potentials of mean force (PMF) (bottom) for wild type glutamine synthetase (GS) (**A**), $GS_{TYN}$ (**B**), and $GS_{TYD}$ (**C**). The reaction

coordinate is the distance *d* between the centers of mass of the phenyl ring of Y336 (or its nitro variants) and the purine ring system of ATP and was sampled for 60 ns for each umbrella window. For the umbrella sampling, a harmonic potential with force constants of 20 kcal $mol^{-1}$ $Å^{-2}$ for distances ≤ 15 Å and 10 kcal $mol^{-1}$ $Å^{-2}$ for distances > 15 Å was applied (schematically depicted by arrows). The PMFs were derived for time intervals of umbrella sampling from zero to 10 ns, zero to 20 ns, and so on.

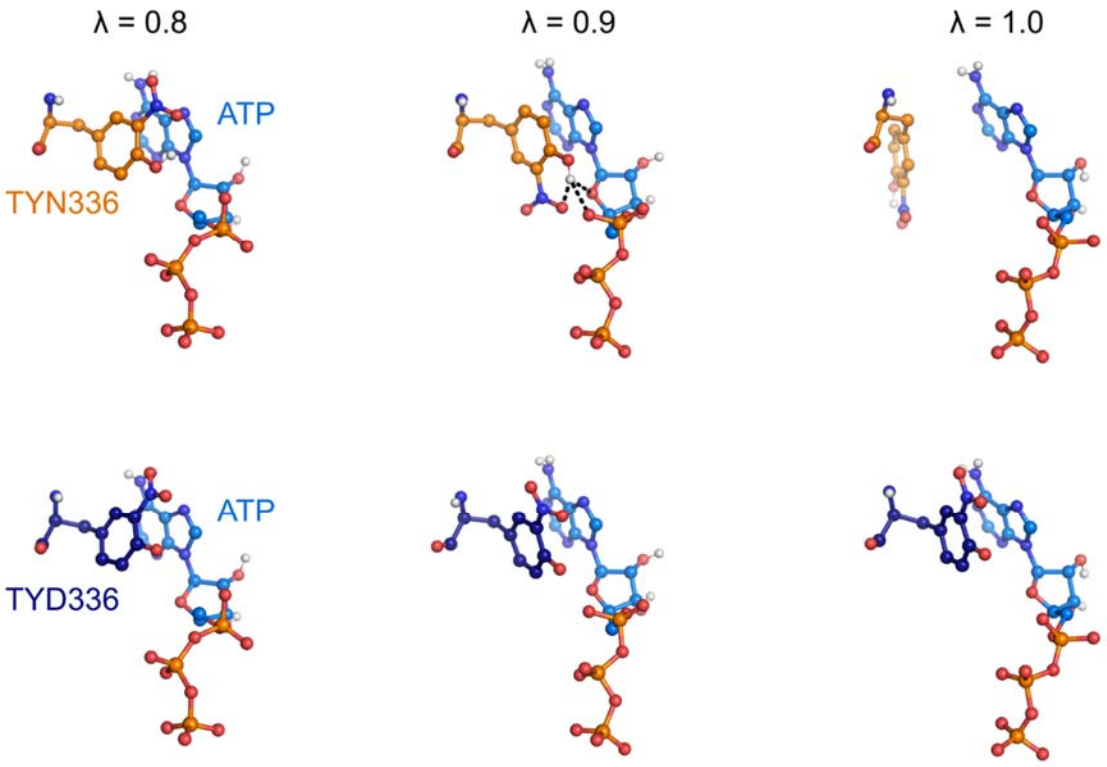


**Figure S11: Conformational analysis of TYN336 and TYD336 side-chains during TI calculations.**
The top row shows representative conformations of TYN336 (orange ball-stick model) and ATP (blue ball-stick model) extracted from TI calculations at λ = 0.8 (left), λ = 0.9 (middle), λ = 1.0 (right). Conformations for TYD366 (dark blue ball-stick model) are shown in the bottom row. At λ = 0.9, the side-chain in TYN336 reorients, such that the $NO_2$-group is now pointing towards the phosphate groups of ATP. This conformation is stabilized by hydrogen bond interactions (black lines) involving the hydrogen atom in the hydroxyl group of TYN336.

# Supplemental Tables

**Table S1. Results from thermodynamic integration simulations.**

**TYN336 into Y336 in the $GS_{ATP}$ state**

| From λ = 0.0 to λ = 1.0 | | | Excl. λ = 0.0 and λ = 1.0 | | |
|---|---|---|---|---|---|
| Time | $\Delta G$[b] | SEM[b,c] | Time | $\Delta G$[b] | SEM[b,c] |
| 3 x 10 | 7.72 | < 0.01 | 3 x 10 | 7.95 | < 0.01 |
| 3 x 20 | 7.75 | < 0.01 | 3 x 20 | 7.89 | < 0.01 |

**TYN336 into Y336 in the $GS_{Apo}$ state**

| From λ = 0.0 to λ = 1.0 | | | Excl. λ = 0.0 and λ = 1.0 | | |
|---|---|---|---|---|---|
| Time[a] | $\Delta G$[b] | SEM[b,c] | Time[a] | $\Delta G$[b] | SEM[b,c] |
| 3 x 10 | 4.84 | < 0.01 | 3 x 10 | 4.75 | < 0.01 |
| 3 x 20 | 4.70 | < 0.01 | 3 x 20 | 4.43 | < 0.01 |

**TYN336 into TYD336 in the $GS_{ATP}$ state**

| From λ = 0.0 to λ = 1.0 | | | Excl. λ = 0.0 and λ = 1.0 | | |
|---|---|---|---|---|---|
| Time[a] | $\Delta G$[b, d] | SEM[b,c] | Time[a] | $\Delta G$[b. d] | SEM[b,c] |
| 3 x 10 | *-56.65* | < 0.01 | 3 x 10 | *-54.97* | < 0.01 |
| 3 x 20 | *-57.67* | < 0.01 | 3 x 20 | *-56.09* | < 0.01 |
| 3 x 30 | *-58.21* | < 0.01 | 3 x 30 | *-56.62* | < 0.01 |

| Excl. λ = 0.9 | | | Excl. λ = 0.0, λ = 0.9, and λ = 1.0 | | |
|---|---|---|---|---|---|
| Time[a] | $\Delta G$[b,e] | SEM[b,c] | Time[a] | $\Delta G$[b,e] | SEM[b,c] |
| 3 x 10 | -62.95 | < 0.01 | 3 x 10 | -61.28 | < 0.01 |
| 3 x 20 | -64.06 | < 0.01 | 3 x 20 | -62.47 | < 0.01 |
| 3 x 30 | -64.62 | < 0.01 | 3 x 30 | -63.04 | < 0.01 |

**TYN336 into TYD336 in the $GS_{Apo}$ state**

| From λ = 0.0 to λ = 1.0 | | | Excl. λ = 0.0 and λ = 1.0 | | |
|---|---|---|---|---|---|
| Time[a] | $\Delta G$[b] | SEM[b,c] | Time[a] | $\Delta G$[b] | SEM[b,c] |
| 3 x 10 | -70.87 | < 0.01 | 3 x 10 | -69.60 | < 0.01 |
| 3 x 20 | -70.69 | < 0.01 | 3 x 20 | -69.30 | < 0.01 |

**ACE-TYN-NME into ACE-TYD-NME in the model systems**

| From λ = 0.0 to λ = 1.0 | | | Excl. λ = 0.0 and λ = 1.0 | | |
|---|---|---|---|---|---|
| Time[a] | $\Delta G$[b] | SEM[b,c] | Time[a] | $\Delta G$[b] | SEM[b,c] |
| 3 x 10 | -68.10 | < 0.01 | 3 x 10 | -67.67 | < 0.01 |
| 3 x 20 | -67.97 | < 0.01 | 3 x 20 | -67.58 | < 0.01 |

[a] in ns and multiples of three replicas

[b] in kcal $mol^{-1}$

[c] SEM: standard error of the mean

[d] $\Delta G$ given in *italics* were not considered for calculation of $\Delta\Delta G$.

[e] Additional bins at λ = 0.85, 0.875, and 0.925 were included to approach the missing bin at λ = 0.9.

**Table S2. Topology and atomic partial charges for TYN**

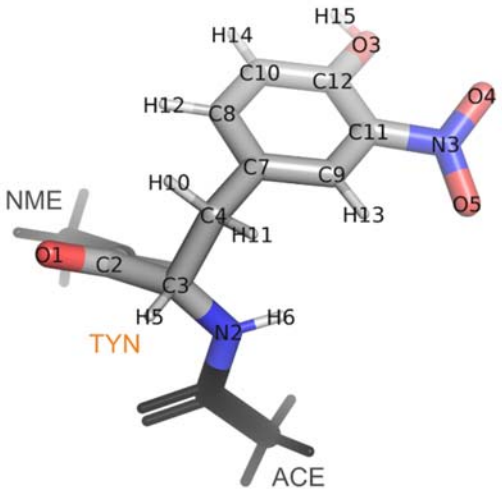


| Atom name | ff99SB atom type | Atomic partial charge |
|---|---|---|
| C2 | C | 0.597300 |
| O1 | O | -0.567900 |
| C3 | CT | 0.101700 |
| N2 | N | -0.415700 |
| H6 | H | 0.271900 |
| C4 | CT | -0.301400 |
| C7 | CA | 0.112150 |
| C8 | CA | -0.085750 |
| C10 | CA | -0.414450 |
| C12 | CA | 0.402900 |
| C11 | CA | -0.113100 |
| C9 | CA | -0.247550 |
| H13 | HA | 0.186350 |
| N3 | NO | 0.877350 |
| O4 | O2 | -0.481600 |
| O5 | O2 | -0.481600 |
| O3 | OH | -0.544700 |
| H15 | HO | 0.434800 |
| H14 | HA | 0.198750 |
| H12 | HA | 0.164050 |
| H10 | HC | 0.120550 |
| H11 | HC | 0.120550 |
| H5 | H1 | 0.065500 |

**Table S3. Force field modifications for TYN**

| #Parameter file for NO2 | | | | |
|---|---|---|---|---|
| **MASS** | | | | |
| NO | 14.010 | 0.530 | | |
| | | | | |
| **BOND** | | | | |
| CA-NO | 322.600 | 1.468 | | |
| NO-O2 | 761.200 | 1.219 | | |
| | | | | |
| **ANGLE** | | | | |
| CA-CA-NO | 66.900 | 119.540 | | |
| CA-NO-O2 | 68.700 | 118.100 | | |
| O2-NO-O2[a] | 76.400 | 127.550 | | |
| | | | | |
| **DIHEDRAL** | | | | |
| X -CA-NO-X | 4.000 | 3.680 | 180.0 | 2 |
| | | | | |
| **IMPROPER** | | | | |
| CA-O2-NO-O2 | | 7.280 | 180.0 | 2 |
| | | | | |
| **NONBON** | | | | |
| NO | 1.824 | 0.170 | | |

[a] As in Amber9 & 10

**Table S4. Topology and atomic partial charges for TYD**

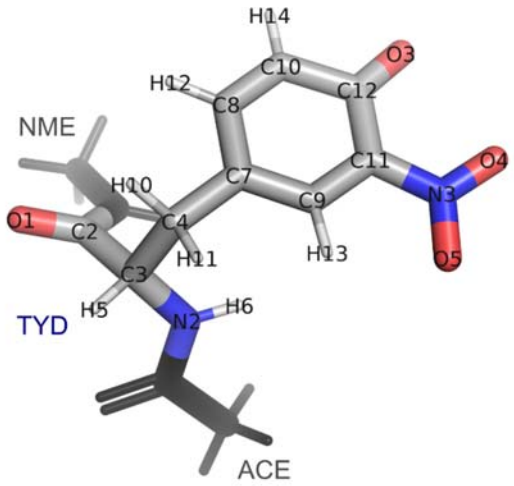


| Atom name | ff99SB atom type | Atomic partial charge |
|---|---|---|
| C2 | C | 0.536600 |
| O1 | O | -0.581900 |
| C3 | CT | 0.206300 |
| N2 | N | -0.516300 |
| H6 | H | 0.293600 |
| C4 | CT | -0.094150 |
| C7 | CA | -0.076900 |
| C8 | CA | -0.051950 |
| C10 | CA | -0.455500 |
| C12 | CA | 0.635950 |
| C11 | CA | -0.228100 |
| C9 | CA | -0.239400 |
| H13 | HA | 0.118100 |
| N3 | NO | 0.804400 |
| O4 | O2 | -0.537600 |
| O5 | O2 | -0.537600 |
| O3 | O | -0.656050 |
| H14 | HA | 0.149750 |
| H12 | HA | 0.150050 |
| H10 | HC | 0.046150 |
| H11 | HC | 0.046150 |
| H5 | H1 | -0.011600 |

**Table S5. Force field modifications for TYD**

| #Parameter file for NO2 | | | | |
|---|---|---|---|---|
| **MASS** | | | | |
| NO | 14.010 | 0.530 | | |
| | | | | |
| **BOND** | | | | |
| CA-NO | 322.600 | 1.468 | | |
| NO-O2 | 761.200 | 1.219 | | |
| CA-O[a] | 570.000 | 1.229 | | |
| | | | | |
| **ANGLE** | | | | |
| CA-CA-NO | 66.900 | 119.540 | | |
| CA-NO-O2 | 68.700 | 118.100 | | |
| O2-NO-O2[b] | 76.400 | 127.550 | | |
| CA-CA-O[c] | 70.000 | 120.000 | | |
| | | | | |
| **DIHEDRAL** | | | | |
| X -CA-NO-X | 4.000 | 7.50 | 180.0 | 2 |
| | | | | |
| **IMPROPER** | | | | |
| CA-O2-NO-O2 | | 7.280 | 180.0 | 2 |
| CA-CA-CA-O[d] | | 1.100 | 180.0 | 2 |
| | | | | |
| **NONBON** | | | | |
| NO | 1.824 | 0.170 | | |

[a] As C-O in parm99.
[b] As in Amber 9 & 10.
[c] As CA-C-OH in parm99.
[d] As CA-CA-C -O in parm99.

# Materials & Methods

## Computational procedures

### Unbiased molecular dynamics simulations

We performed unbiased molecular dynamics (MD) simulations of the human glutamine synthetase (GS) bound to ATP and magnesium ions ($Mg^{2+}$) with water represented explicitly, using the Amber 14 and 16 software suits[6-7]. The ATP-bound state (further referred to as $GS_{ATP}$) was previously used by us to determine the molecular consequences of mutations on structural and energetic features of GS[8], and a detailed preparation protocol is reported therein. In short, as to GS, all simulations were started from a dimeric model of human GS extracted from PDB-ID 2QC8[1]. ATP and $Mg^{2+}$ replaced cocrystallized and structurally bound ADP and manganese ions, such that the additional γ-phosphate group of ATP is oriented towards the center of the binding site.

We also prepared an *apo* state, in which ATP is missing (further referred to as $GS_{Apo}$). Hydrogen atoms not present in the crystal structure were added according to the ff99SB library[9-10]. Afterward, to introduce residue TYN336 (referred to as $GS_{TYN}$) and TYD336 (referred to as $GS_{TYD}$), we adapted the coordinates of the wild type residue Y336. As there is no information available as to which rotamer state of the phenyl ring of TYN336 or TYD336 is preferred in the GS, we performed 3 × 100 ns MD simulations in the $GS_{Apo}$ state for $GS_{TYN}$ and $GS_{TYD}$, in which we initially placed the nitro group in positions ① or ② (**Figure S7A**). We used the dihedral $\alpha$ (**Figure S7A**) as a measure to investigate the relative orientation of the nitro group over the MD trajectory. The shape of the density curves is similar over both GS variants and reveals two peaks, one at $\alpha \approx -90°$ and one at $\alpha \approx 90°$, corresponding to orientations ① and ②, respectively (**Figure S7B**). Considering the uncertainty in the calculations, the occurrence frequencies of the two orientations ① and ② do not differ significantly. Taking into consideration that the nitro group in position ① is pointing towards the top of the ATP binding site and in position ② towards the center of the binding site, we used orientation ① as a starting orientation for further MD simulations. Note that except for the nitro group in $GS_{TYN}$ and $GS_{TYD}$ and the missing hydrogen atom in $GS_{TYD}$, the initial coordinates for the $GS_{ATP}$ structure were otherwise identical throughout all GS variants. Finally, the complex structures were solvated by TIP3P water[11] using a truncated octahedron and leaving at least 11 Å between the solute and the edge of the box and neutralized by sodium counter ions.

Atomic partial charges for protein residues were taken from the ff99SB force field[9-10]. As to residues TYN and TYD, the atomic partial charges were derived according to the *RESP* procedure[12-13] (**Table S2 and S4**). Torsion parameters for the nitro group were taken from the library from Myung *et al.*[14] (**Table S3 and S5**). All other force field parameters were taken from the ff99SB force field[9-10] (**Table S3 and S5**). As to ATP and $Mg^{2+}$, atomic partial charges and force field parameters were taken from the libraries of Meagher *et al.*[15] and Allner *et al.*[16], respectively. All simulations were performed using GPU acceleration with the *pmemd.cuda* module implemented in Amber[17].

The general simulation protocol was adapted from ref.[8]. After energy minimization, thermalization, and density adaptation, the $GS_{ATP}$ structures for wild type GS, $GS_{TYN}$, and $GS_{TYD}$ were subjected to 5 × 500 ns of unbiased MD simulations. We varied the target temperature during equilibration from 299.8 K – 300.2 K in 0.1 K intervals. This procedure results in slightly different starting structures for subsequent production simulations, such that the resulting trajectories can be considered independent.

**The structural integrity of the dimeric model of human GS and convergence test**

We computed the root mean square deviation (RMSD) average correlation (RAC)[18] for all protein backbone atoms using *cpptraj*[19] to determine the timescale of structural changes observed during MD simulations[18]. The RAC curves decrease smoothly during 500 ns of MD simulations, although we find small bumps in one trajectory for each GS variant (**Figure S8**), indicating small structural changes. RAC curves computed for $GS_{core}$[8] residues (disregarding the 10% of the most mobile amino acids[8]) also decrease smoothly but without showing any bumps (**Figure S9**). Thus, the bumps arose from structural changes in those regions where the adjacent subunit of the full-length GS is missing, as pointed out previously[8]. However, as these changes do not influence the binding site, which is part of $GS_{core}$, we conclude that our structural models are appropriate to study the influence of tyrosine nitration on ATP binding.

**Geometric parameters to monitor the influence of tyrosine nitration on ATP binding**

To monitor the influence of tyrosine nitration on ATP binding directly, the MD trajectories were analyzed towards structural features that characterize stacking interactions between ATP and

residue 336. We measured, first, the distance between the geometric centers of the benzene ring in residue 336 and the purine ring in ATP, and, second, the angle between both ring planes. The results are expressed as mean relative frequencies ± standard error of the mean (SEM) over five trajectories, normalized to the sum of all bins. Additionally, we computed the root mean square fluctuation (RMSF), relative to the average structure, as a measure for ATP mobility in the binding site, after superimposing all $GS_{core}$ backbone atoms to the average structure.

**Computation of effective binding energies**

After the MD simulations, we computed effective binding energies[20-21] for ATP by the molecular mechanics Poisson-Boltzmann surface area (MM-PBSA) approach[22-23]. The general settings were adapted from our previous study[8].

The computations were performed with Amber 16[24] considering configurations sampled at an interval of 100 ps (i.e., 5 × 5000 each) along the MD trajectories. Calculations were performed considering ATP as the ligand and the protein structure and structurally bound ions as the receptor. We applied the 1-trajectory MM-PBSA approach, in which the snapshots of the complex, receptor, and ligand are extracted from a single MD simulation of the complex[22]. To avoid any additional uncertainty in our calculation, we neglected contributions due to changes in the configurational entropy upon complex formation[20, 25]. The effective binding energies ($\Delta G_{effective}$) were averaged over five trajectories ($\overline{\Delta G}_{effective}$). Relative effective binding energies ($\Delta\Delta G_{effective}$) were calculated by subtracting the mean $\Delta G_{effective}$ of the wild type ($\overline{\Delta G}_{wild\ type}$) from the effective binding energy of the nitro variant ($\overline{\Delta G}_{nitro}$) (eq. (1)).

$$\Delta\Delta G_{effective} = \overline{\Delta G}_{nitro} - \overline{\Delta G}_{wild\ type} \quad (1)$$

The SEM over the five independent MD simulations for a system ($SEM_{1\text{-}5}$) was calculated by error propagation according to eq. (2)

$$SEM_{1\text{-}5} = \frac{1}{5}\sqrt{\sum_{i=1}^{5} SEM_i^2} \quad (2)$$

where $SEM_i$ is the SEM for trajectory $i$. The total SEM ($SEM_{total}$) was then calculated by error propagation according to eq. (3)

$$SEM_{\text{total}} = \frac{1}{2}\sqrt{(SEM_{1\text{-}5}^{\text{nitro}})^2+(SEM_{1\text{-}5}^{\text{wild type}})^2} \quad (3)$$

where $SEM_{1\text{-}5}^{\text{nitro}}$ is the SEM over five trajectories for a 3-nitro variant and $SEM_{1\text{-}5}^{\text{wild type}}$ the SEM over five trajectories for wild type GS. The results are expressed as $\Delta\Delta G_{\text{effective}} \pm SEM_{\text{total}}$. Additionally, the $\Delta G_{\text{effective}}$ values are expressed as mean distribution $\pm SEM_{1\text{-}5}$, normalized to the sum of all bins.

**Thermodynamic integration simulations**

Thermodynamic integration (TI) simulations estimate the free energy difference between two states employing a non-physical, alchemical pathway[26-28]. Therefore, the coupling parameter $\lambda$, which ranges from $\lambda = 0$ to $\lambda = 1$, is introduced that connects the potential energy functions $V$ of both states[29]. In practice, the transformation simulations are broken down into a series of multiple values of $\lambda$[29].

We followed the TIES strategy[30] (**T**hermodynamic **I**ntegration with **E**nhanced **S**ampling) and performed the alchemical transformation at 13 discrete $\lambda$-steps ($\lambda$ = 0.0, 0.05, 0.1, 0.2, …, 0.9, 0.95, 1.00), applying the one-step softcore approach[31-32]. Technically, we simulated the transformation of TYN336 into Y336 and TYN336 into TYD336 in the $GS_{APO}$ and $GS_{ATP}$ states. For TI simulations of TYN336 into TYD336 in the $GS_{ATP}$ state, additional simulations at $\lambda$ = 0.85, 0.875, and 0.925 were performed. In the cases of transformations including TYD, the absolute charge of the system changed during transformation, such that we applied a uniform neutralizing plasma to reach electroneutrality[33]. For each $\lambda$-step, we performed an independent energy minimization, thermalization towards 300 K, and density adaptation towards 1 bar. From here, we started three independent replica simulations[30], in which the initial velocities were randomly assigned during the first step of the simulation. After ten ns equilibration simulation, we started to record the $\Delta V/\Delta\lambda$ potentials[26-28]. The average $\Delta V/\Delta\lambda$ values for each $\lambda$-step are calculated as an ”ensemble average approach”, referring to performing three independent simulations to calculate averaged free energies[30, 34-35]. The average $\Delta V/\Delta\lambda$-curves (**Figure S3**) are finally integrated from $\lambda = 0$ to $\lambda = 1$, yielding free energy difference $\Delta G$ for the transformation. Employing the principles of a thermodynamic cycle[36-37] (see main text **Figure 4A**), relative free energies of ATP binding ($\Delta\Delta G_{\text{bind.}}$) are calculated according to eq (4)

$$\Delta\Delta G_{\text{bind.}} = \Delta G_{\text{ATP}} - \Delta G_{\text{Apo}} \quad (4)$$

where $\Delta G_{\text{ATP}}$ and $\Delta G_{\text{Apo}}$ denote the free energy changes in the $GS_{ATP}$ and $GS_{Apo}$ state, respectively.

Energy minimization, thermalization, and density adaptation were performed by employing the MPI version of TI in Amber 18[38]. The *NPT* equilibration and production simulations were performed by using the CUDA version of TI[39-40] in Amber 18[38]

In 10 ns intervals, we evaluated the convergence of the systems. The simulations are considered as approximately converged, if, first, the SEM for each $\lambda$-step is < 0.01 kcal mol$^{-1}$, second, the SEM for $\Delta G$ is < 0.01 kcal mol$^{-1}$, and, third, the change in $\Delta G$ to the previous 10 ns is < 0.5 kcal mol$^{-1}$. The simulation times and $\Delta G \pm$ SEM are summarized in **Table S1**. The total error for $\Delta\Delta G_{\text{bind.}}$ was then calculated analogously to eq. (3).

**Potential of mean force calculations**

To investigate a potential influence of Y336 nitration on the binding kinetics of ATP, we performed the potential of mean force (PMF) calculations of ATP unbinding from its binding site within wild type GS, $GS_{TYN}$, and $GS_{TYD}$. We computed the PMF (configurational free energy) of ATP unbinding employing umbrella sampling[41] and the Weighted Histogram Analysis Method (WHAM)[42].

To do so, we, initially, simulated the ATP unbinding path starting from the ATP-bound, minimized wild type GS structure by determining a vector for the unbinding path by random acceleration (expulsion) MD[2]. ATP was then translated along this vector in 0.5 Å steps (**Figure S4A**). The complete unbinding path covers a distance of ~37 Å, divided into 75 windows/umbrellas. In the unbound state, there is at least a distance of 12 Å between ATP and the protein structure (**Figure S4A**). Note that, similarly to our unbiased MD simulations, the starting structures for wild type GS, $GS_{TYN}$, and $GS_{TYD}$ differ only in position 336.

As a reaction coordinate, we used the distance *d* between the centers of mass of Y/TYN/TYD336's benzene ring and ATP's purine ring (**Figure S4B**). Umbrella sampling MD simulations were performed applying harmonic potentials with a force constant of 20 kcal mol$^{-1}$ Å$^{-2}$ for $d \leq 15$ Å and 10 kcal mol$^{-1}$ Å$^{-2}$ for $d > 15$ Å. During umbrella sampling simulations, we applied positional

restraints on backbone atoms of residues 211 – 231 of both subunits (**Figure S4A**) to ensure a constant relative orientation of the protein structure. Of primary importance in the selection of these residues was that they are located in the center of each subunit, but do not interfere with the binding site or binding pathway. This setup led to Gaussian-shaped frequency distributions for each reference point along the reaction coordinate, with all such distributions well overlapping (**Figure S10**). WHAM was used to derive the PMF from these distributions[42]. The uncertainty was determined by bootstrapping and is always < 0.05 kcal mol$^{-1}$, if not reported differently. The PMFs are qualitatively indistinguishable after 60 ns of umbrella sampling simulations (**Figure S10**). In addition, when extending the simulation time from 50 ns to 60 ns, the changes in the PMFs are ≤ 0.76 kcal mol$^{-1}$. Thus, both results suggest converged PMFs. Transitions in terms of changes in configurational free energy along *r* are reported as $\Delta G_{d\,\text{Å} \rightarrow d+x\,\text{Å}}$ (in kcal mol$^{-1}$), where *x* represents the change of *d* in Å.

**Calculating p$K_a$ shifts from free energies**

To calculate the p$K_a$ shift of TYN336 due to the protein environment, we applied the method reported by Simonson *et al.*[43]. The calculation is based on the relation of the equilibrium constant $K_a$ and the standard free energy $\Delta G$ (eq. (5))

$$\Delta G = -RT \ln K_a \tag{5}$$

where $R$ is the gas constant of 0.001987 kcal mol$^{-1}$ K$^{-1}$ and $T$ = 300 K. Eq. 4 can be alternatively expressed as eq. (6)

$$\text{p}K_a = -\log K_a = \frac{1}{2.303\,RT}\Delta G \tag{6}$$

and eq. (7)

$$\text{p}K_{a,\text{prot.}} = \text{p}K_{a,\text{ model}} + \frac{1}{2.303\,RT}\Delta\Delta G \tag{7}$$

where p$K_{a,prot}$ and p$K_{a,model}$ are the p$K_a$'s of TYN336 in the protein and free TYN in solution, respectively. $\Delta\Delta G$, the difference in free energy between two states, is calculated according to eq. (8)

$$\Delta\Delta G = \Delta G_{\text{prot.}} - \Delta G_{\text{model}} \quad (8)$$

The individual error for $\Delta G_{\text{prot}}$ and $\Delta G_{\text{model}}$ was estimated by simple additive error propagation, and the total error for $\Delta\Delta G$ was then calculated analogously to eq. (3)

We used TI (for technical details, please see above) to calculate $\Delta G$ for the transformation of TYN into TYD in our model structure and TYN336 into TYD336 in the $GS_{Apo}$ structure (**Figure 6A**).

**Analysis of results**

If not reported differently, results are expressed as mean values ± SEM and compared using a two-sided Student´s *t*-test (using the R software[44]). *P* values < 0.05 were considered statistically significant.

**Experimental procedures**

**Materials**

The monoclonal antibody directed against human GS, clone 6) was from Beckton-Dickinson (Heidelberg, Germany). The monoclonal antibody against 3´-nitrotyrosine was from Upstate Biotechnologies (Thermo Fisher, Heidelberg, Germany). Horseradish peroxidase-coupled goat anti-mouse IgG antibodies were from Biorad International (Munich, Germany). Peroxynitrite ($ONOO^-$), KOH, and $KH_2PO_4$ were from Merck Millipore (Darmstadt, Germany). Imidazole, sodium glutamate, adenosine 5´-triphosphate, phosphoenolpyruvate, magnesium chloride, potassium chloride, ammonium chloride, ß-nicotinamide adenine, pyruvate kinase and L-lactic dehydrogenase were from Sigma (Deisenhofen, Germany). Bovine serum albumine was from Roche (Mannheim, Germany).

**Expression and purification of human glutamine synthetase**

A plasmid expressing human GS was donated to us by Dr. Norma Allewell and used to transform *E. coli* and to express the enzyme in these cells, as described by Listrom *et al*.[45]. The subsequent of human GS was adapted from the methods published by Listrom *et al*.[45]. In brief, the clarified sonicates of *E. coli* suspensions expressing human GS underwent successive purification on HA

Ultrogel®, DEAE-Sepharose, and MonoQ resins, using linear: 100 to 500 mM potassium phosphate buffer (pH 7.2), step: imidazole-NaOH at pH 7.9, and linear: 0 to 250 mM NaCl in 20 mM Tris-HCl, respectively. The potassium phosphate buffer also contained 5 mM 2-mercaptoethanol. Similarly, the imidazole-NaOH buffers also contained 1 mM EDTA and 5 mM 2-mercaptoethanol. The first two separations were performed at room temperature, while the final chromatography was carried out at 4°C and yielded a protein that was > 99% pure as judged by SDS-PAGE. The purified human GS was combined with glycerol at a final concentration of 10% and stored at 4°C. GS activity during the purification was assessed using hydroxamate assay, as described by Jeitner and Cooper[46]. The reaction mixture for this assay consists of enzyme and 100 mM Tris-HCl (pH 7.4), 100 mM hydroxylamine, 10 mM ATP, 10 mM $MgCl_2$, 10 mM glutamate, and 2 mM dithiothreitol in a volume of 55 µl. Incubations were carried out at 37°C for periods up to 45 min and terminated with the addition of 165 µl of 0.37M $FeCl_3$, 0.67 M HCl, and 0.2 m trichloroacetic acid per 55 µl reaction. These mixtures were then centrifuged at 10,000 x g for ten minutes at 4°C and the absorbance of 200 µl of the supernatant fraction at 535 nm recorded. γ-Glutamylhydroxamate formation was calculated using an extinction coefficient of 850 $M^{-1}$ $cm^{-1}$.

**Peroxynitrite treatment of human glutamine synthetase**

Purified human GS was incubated in 0.1 M $KH_2PO_4$ (pH 7.0) and nitrated by the addition of peroxynitrite ($ONOO^-$, in 0.1 M KOH) under constant stirring as described before[47]. Samples were stirred for 5 s and incubated on ice for another 30 min. Final $ONOO^-$ concentrations were 5, 50, 100 and 200 µM. For $ONOO^-$-free control, GS was exposed to vehicle only (0.1 M KOH). Aliquots from the reaction mixture were taken for Western blot analysis of 3´-nitrotyrosine or GS and determination of enzyme activity as described below.

**Western blot analysis**

Western blot analysis was performed as described before[47]. Briefly, equal amounts of isolated human GS were subjected to sodium dodecyl sulfate-polyacrylamide gel electrophoresis (SDS-PAGE) using 10% gels. Proteins were transferred onto nitrocellulose membranes by semi-dry blotting (BioRad, Munich, Germany). Membranes were washed in Tris-buffered saline containing 0.1% Tween20 (TBS-T) and incubated in TBS-T containing 10% bovine serum albumin (BSA) for

30 min. At the end of the incubation time, blots were probed for 2 h at room temperature with antibodies against 3´-nitrotyrosine (mAb, Upstate) or GS (mAb, Becton Dickinson, 1:5,000) diluted in TBS-T + 5% BSA. Blots were washed three times and incubated in TBS-T + 5% BSA containing horseradish peroxidase-coupled antibodies directed against mouse immunoglobulins (1:10,000, 2 h, RT). Peroxidase activity on the membranes was detected using Western-Lightning chemiluminescence reagent plus (Perkin Elmer, Waltham, USA). Digital images were captured using the ChemiDoc MP and Image Lab software (Biorad, München, Germany).

**Glutamine synthetase activity assay**

Human GS activity was measured according to ref. [48] by using a commercial kit (SPGLUT11, Sigma, Deisenhofen, Germany). In this assay, the conversion of ATP to ADP by GS is coupled to the oxidation of NADH to $NAD^+$ by L-lactic dehydrogenase. The final reaction mixture contained 34.1 mM imidazole, 102 mM sodium glutamate, 8.5 mM adenosine 5´-triphosphate, 1.1 mM phosphoenolpyruvate, 60 mM magnesium chloride, 18.9 mM potassium chloride, 45 mM ammonium chloride, 0.25 mM ß-nicotinamide adenine, 28 units pyruvate kinase and 40 units L-lactic dehydrogenase. The pH of the reaction mixture was adjusted to pH 7.0, 6.0 or 4.0 before the reaction was initiated by the addition of purified GS. The reaction mixture was incubated for ten min at 37°C, and the absorbance was measured at 340 nm using a spectrophotometer (UV-2600, Shimadzu, Duisburg, Germany). GS activity in $ONOO^-$-exposed samples is expressed relative to vehicle-treated control at pH 7.0.

**Analysis of results**

Experiments were repeated three times, and results are expressed as arithmetic means ± SEM. Statistical analysis was performed using one-way analysis of variance (ANOVA) followed by Tukey´s multiple comparison *post hoc* test (Graph Pad Prism, Prism, USA). $P$ values < 0.05 were considered statistically significant.

## Supplemental Notes

### Assessment of computational procedures

In this study, we have shown by molecular dynamics (MD) simulations and end-point, pathway, and alchemical transformation free energy calculations that Y336 nitration in human glutamine synthetase (GS) hampers substrate (ATP) binding if nitrated Y336 is in the deprotonated, negatively charged TYD336 state. Here, we argue that our computations allow drawing this conclusion.

Human GS is composed of ten identical subunits that form two pentameric rings in which the C-terminus of one monomer interacts with the N-terminus of the adjacent monomer[1] (**Figure 1A**). The catalytic active site is located in the interface of two neighboring subunits and, thus, full-length GS contains ten identical catalytic sites[1]. In this study, to keep computational costs manageable, we used a dimeric GS model that includes a single catalytic site in its dimerization interface. Previously, we showed that our dimeric GS model allows performing MD simulations in a computationally efficient way, relative to the decameric GS structure, without loss in quality[8]: Over the course of the MD simulations, the recorded structural deviations (measured as root mean square deviation (RMSD)) in the binding site region of the dimeric system were always < 1 Å and similar to the structural deviations found for the decameric structure[8]. As Y366 is part of the nucleotide-binding site, Y336 thus does not undergo large structural deviations either. Furthermore, Y336 does not contribute to interface protein-protein interactions in human GS[49]. By contrast, Y366 is directly interacting with ADP in the crystal structure[1] (**Figure 1A**). We thus feel it safe to assume that the inhibitory effect of Y336 nitration originates from hampered substrate binding rather than changes in the GS oligomer stability. Overall, our dimeric GS model should be appropriate to study the influence of Y336 nitration on substrate binding in a computationally efficient way.

We used well-established force field parameters to describe the dynamics of proteins[9-10], ions[15], nucleotides[16], and solvent[11], but we note that more recent protein force fields have become available[50-51]. The force fields follow a classical mechanical representation of stacking interactions with a fixed-charge force field[52]. We note that stacking interactions described by the Amber type force field[53], as used here, have been shown to be in good agreement with stacking interactions described by sophisticated and physically complete quantum mechanical calculations[54-57]. The impact of force field deficiencies on our results is expected to be negligible due to cancellation of errors when comparatively assessing the structural and energetic features of nitrated GS (TYN or

TYD variant) relative to wild type GS. We paid particular attention to the parameters describing TYN and TYD. Parameters for the protonated, neutral TYN variant have been reported by Myung and Han[14], but structural parameters and atomic partial charges for the deprotonated, negatively charged TYD variant were not available at the beginning of this study. Initial molecular mechanics (MM) minimizations of different ACE-TYD-NME structures showed a significant rotation of the $NO_2$ group relative to the ring plane, whereas the $NO_2$ group was almost in a plane with the ring in QM-optimized structures. Therefore, parameters for the torsion angle C-C-N-O in the TYD state were newly derived. Besides, to ensure consistency of the charge determination procedure, charges for both TYN and TYD were (re-)determined. To do so, we used model peptides of TYN and TYD that were capped by acetyl (ACE) and *N*-methyl (NME) groups. In conformity with the proceedings for charge determination of amino acids in the Cornell *et al.* force field[9], two conformers representing an α-helical and β-strand conformation were prepared. We also considered that the nitro group can be either oriented towards the ACE or NME group. A multi conformer least-squares-fitting procedure derived atomic partial charges. In the end, for MD simulations of the TYN variant, we used the force field parameters of Myung and Han[14] with atomic partial charges computed here, and for MD simulations of the TYD variant, we used ff99SB atom types with optimized C-C-N-O torsion angle parameters and atomic partial charges calculated here. All relevant force field parameters applicable to the Amber ff99SB force field[9-10] are provided in **Table S2-S5.**

That Y336 nitration in human GS hampers substrate (ATP) binding, but only in its deprotonated and negatively charged TYD336 state, has been demonstrated by four independent ways. First, we studied the structural features upon tyrosine nitration by unbiased MD simulations, which allows to study the structural dynamics at high temporal and spatial resolution in full atomic detail[58]. For investigating the effects Y336 nitration, we followed an "ensemble average approach"[34, 39, 59-60] in that five independent MD simulations were performed for dimeric wild type GS and nitrated GS in its protonated, neutral $GS_{TYN}$ state and deprotonated, negatively charged $GS_{TYD}$ state, respectively. This procedure allows, first, to test for the influence of different starting conditions and, second, to determine the statistical uncertainties of the computed results[18, 61]. We, initially, computed the RMS average correlation (RAC)[18] for all protein backbone atoms to determine the timescale of structural changes observed during MD simulations[18] (**Figure S8**). These RAC curves generally decrease smoothly during 500 ns of MD simulations, although we find small bumps in

one trajectory for each GS variant, indicating small structural changes there. RAC curves computed for $GS_{core}$[8] residues (disregarding the 10% of the most mobile amino acids[8]) also decrease smoothly but without showing any bumps (**Figure S9**). Thus, the bumps arose from structural changes in those regions where the adjacent subunit of the full-length GS is missing, as pointed out previously[8]. However, as these changes do not influence the binding site, which is part of $GS_{core}$, we again conclude that our structural models should be appropriate to study the influence of tyrosine nitration on the interaction with ATP.

Second, we analyzed the energetic consequences upon tyrosine nitration on substrate binding by the molecular mechanics Poisson-Boltzmann surface area (MM-PBSA) approach[22-23] (**Figure 3**). The MM-PBSA approach is an end-point free energy calculation method and allows us to estimate the absolute free energy of binding a ligand, here ATP, to a receptor, here human GS [22, 62]. We followed the 1-trajectory approach, such that all coordinates were extracted from MD ensembles of the complex structure[22, 62]. In contrast to the 3-trajectory approach[22], the 1-trajectory approach requires fewer simulations but neglects any changes of the ligand and receptor structure upon binding[62]. However, there is evidence that suggests that the 1-trajectory approach, in practice, often gives more accurate results compared to the 3-trajectory approach, probably due to the cancellation of errors and the limited sampling in the 3-trajectory approach[62-65]. Previous studies showed that the inclusion of configurational entropy is crucial for calculating absolute binding free energies[25, 62]. In this study, however, we are rather interested in relative changes upon tyrosine nitration to wild type GS and, thus, we decided to neglect contributions due to changes in the configurational entropy of the ligand or the receptor upon complex formation, to avoid introducing additional uncertainty in the computations[20, 25, 66]. We considered five trajectories for each GS system for free energy calculations, as previous studies suggest that multiple "short" trajectories efficiently produce converged free energy estimates and meaningful error estimates[39, 67-69]. As recommended for MM-PBSA calculations, we used Parse radii[70] to calculate the polar part of solvation free energies[21]. In MM-PBSA calculations, the electrostatic contribution depends on the solute dielectric constant $\varepsilon$[62], and for a highly charged binding interface, a higher solute dielectric constant is preferred[25]. Often best results are observed for $\varepsilon = 2 - 4$[25, 62, 71-72]. In human GS[1], we are facing a highly polar and charged binding site, including six negatively charged residues (E134, E136, E196, E203, E305, and E338), five positively charged residues (K43, R45, R319, R324, and R340),

at least two structurally bound $Mg^{2+}$ ions, and the negatively charged phosphate groups of ATP, such that we set $\varepsilon = 4$.

Third, we computed relative binding free energies ($\Delta\Delta G_{bind.}$) for ATP binding according to eq. (4). For this, $\Delta\Delta G_{bind.}$ was computed by evaluating the thermodynamic cycle (**Figure 4A**) by means of TI[21, 73]. Additionally, we computed the p$K_a$ shift of TYN336 relative to (free) 3-nitro tyrosine according to eq. (5) - (7). For this, $\Delta\Delta G$ was computed by evaluating the thermodynamic cycle (**Figure 6A**). Technically, we simulated the transformation of TYN336 into Y366, TYN366 into TYD336, or ACE-TYN-NME into ACE-TYD-NME, as we expect that the $\Delta V/\Delta\lambda$ potentials converge faster when removing $NO_2$ group (TYN → Y) or a hydrogen atom (TYN → TYD) from the system instead off simulating the formation of these atoms. In the cases of transformations including TYD, the absolute charge of the system changed during transformation, such that we applied a uniform neutralizing plasma to reach neutrality[33]. In general, TI employs a non-physical, alchemical pathway and the changes along this pathway are usually smaller and converge, thus, faster compared to the physical realistic association pathways[37], in which also slow desolvation processes[74] and substantial conformational changes must be considered. For TI calculations, however, sufficient sampling is critical for the accuracy of the results[28], which is why we followed the TIES strategy[30]. In detail, the alchemical pathway was decomposed into 13 individual λ-steps and, in general, the accuracy of TI calculations can be increased by increasing the number of individual λ-step, however, so does the computational costs[29]. Another key feature of the TIES strategy[30] is that multiple, independent replica simulations are performed in the sense of an "ensemble average approach"[34, 39, 59-60]. Over the recent years, various studies provide evidence that suggests that multiple short simulations provide much more reasonable binding free energies and error estimates than running a single long simulation[67-69, 75-76]. Because of the high computational costs of TI computations, we intended to keep the simulation time per λ-step as short as possible. We thus increased the sampling time, for which we recorded the $\Delta V/\Delta\lambda$ potentials, in intervals of 10 ns. For transformations not involving TYD336, $\Delta G$ changed only marginally when increasing the sampling time from 3 × 10 ns to 3 × 20 ns (**Figure S3**). As to transformations considering TYD336 sampling intervals of 3 × 30 ns were needed, likely due to additional charged in TYD336 (**Figure S3**). This data, thus, suggests that the computations can be considered converged.

In the present study, we performed one-step softcore TI calculations, in which the van der Waals and electrostatic interactions are simultaneously modified.[31] In general, the one-step TI calculations can be considered computationally less expensive compared to the two-step TI calculations, in which both properties are modified separately.[31] In one-step TI calculations, however, care must be taken when kinks appear in the $\Delta V/\Delta\lambda$ curve, which is known to decrease the accuracy of the calculations[31]. In the present study, such a kink was found at $\lambda = 0.9$ when simulating the transformation of TYN366 into TYD336 in the $GS_{ATP}$ state (**Figure S3C**). At this point in the transformation, the side-chain in TYN336 reorients, such that the $NO_2$-group is now oriented towards the phosphate-groups of ATP (**Figure S11**). By contrast, at $\lambda = 0.8$, TYN336 and ATP are still oriented in parallel, and at $\lambda = 1.0$, TYN is physically not present and its side-chain is allowed to move freely. Hence, this orientation is unique for $\lambda = 0.9$. In the flipped TYN336 conformation, TYN336 is stabilized by hydrogen bonds involving the hydrogen atom of the hydroxyl group in TYN336, which is a plausible explanation for the kink in the $\Delta V/\Delta\lambda$ curve at $\lambda = 0.9$ (**Figure S3C**). We, thus, decided to approach $\lambda = 0.9$ by additional simulations at $\lambda = 0.85$, 0.875, and 0.925, and the average $\Delta V/\Delta\lambda$ potentials well integrats into the $\Delta V/\Delta\lambda$ curve (**Figure S3C**). Consequently, we considered $\lambda = 0.85$, 0.875, and 0.925 but not $\lambda = 0.9$ for the calculations of $\Delta G$ and $\Delta\Delta G$, respectively.

Fourth, we determined the influence of Y336 nitration on the actual binding process of ATP. Applying MD simulations of free ATP diffusion in the presence of the GS to reconstruct the binding pathway that way[60, 77] did not seem suitable to us in this case given the high binding affinity of ATP to GS ($K_M$ = 1.8 mM[45]) and, hence, the expected low off-rate. We, thus, decided to perform potential of mean force (PMF) calculations of ATP (un-)binding from its binding site within the GS variants. We computed the PMF for ATP (un-)binding employing umbrella sampling[41] and the Weighted Histogram Analysis Method (WHAM)[42], as this combination was successfully applied by us previously[78-80] and is expected to suffer less from relaxation problems in complex systems such as protein-ligand systems[81]. Technically, we simulated the ATP unbinding path, starting from the ATP-bound GS model that was used for prior MD simulations. That way, we avoid introducing any uncertainties that arose from arbitrarily placed ATP outside of the binding site. Instead, we determined a vector that describes a linear unbinding path by random acceleration (expulsion) MD[2], and ATP was then translated along this vector in 0.5 Å steps (**Figure S4**). The complete unbinding path covers a distance of ~37 Å, divided into 75 windows (**Figure S4**). In the completely

unbound state, the minimal distance between any atom in ATP and any atom in Y336 is 23.6 Å, such that ATP can move without any bias from Y336 in the completely unbound state. Note that the starting structures for wild type GS, $GS_{TYN}$, and $GS_{TYD}$ differ only in position 336, such that any relative change of the PMF between the variants are highly likely the consequence of nitrated Y336 and not biased by the initial coordinates. During umbrella sampling simulations, we restrained the distance between the centers of mass of Y336/TYN336/TYD336's benzene ring and ATP's purine ring as an intuitive reaction coordinate. For all GS variants, we obtained Gaussian-shaped frequency distributions for each umbrella sampling simulation along the reaction coordinate, with all such distributions well overlapping, which is a prerequisite for the subsequent derivation of the PMF[82].

Considering that the specified reaction coordinate is the same in all three cases of ATP (un-) binding from wild type GS, $GS_{TYN}$, or $GS_{TYD}$ and that the sampled unbound state is very similar in all three cases (as qualitatively shown in **Figure 5B**), differences in the PMFs relative to the unbound state indicate differences in the binding energetics among the three systems. In that respect, it is encouraging that differences in the PMF values of the bound state between wild type GS and both nitrated GS variants (**Figure 5A**) are in very good agreement with results from MM-PBSA calculations (**Figure 3A**) and TI simulations (**Figure 4**), both qualitatively and quantitatively. Thus, the results from the PMF computations also provide internal validation of our MM-PBSA calculations and TI simulations and *vice versa*.

## Supplemental References


1. Krajewski, W. W.; Collins, R.; Holmberg-Schiavone, L.; Jones, T. A.; Karlberg, T.; Mowbray, S. L., Crystal structures of mammalian glutamine synthetases illustrate substrate-induced conformational changes and provide opportunities for drug and herbicide design. *J. Mol. Biol.* **2008,** *375* (1), 217-28.
2. Ludemann, S. K.; Lounnas, V.; Wade, R. C., How do substrates enter and products exit the buried active site of cytochrome P450cam? 1. Random expulsion molecular dynamics investigation of ligand access channels and mechanisms. *J. Mol. Biol.* **2000,** *303* (5), 797-811.
3. Bartesaghi, S.; Campolo, N.; Issoglio, F.; Zeida, A.; Grune, T.; Estrín, D.; Radi, R., Oxidative inactivation of human glutamine synthetase: biochemical and computational studies. *Free Radic. Biol. Med.* **2016,** *100*, S19.
4. Görg, B.; Wettstein, M.; Metzger, S.; Schliess, F.; Häussinger, D., Lipopolysaccharide-induced tyrosine nitration and inactivation of hepatic glutamine synthetase in the rat. *Hepatology* **2005,** *41* (5), 1065-1073.
5. Görg, B.; Wettstein, M.; Metzger, S.; Schliess, F.; Häussinger, D., LPS-induced tyrosine nitration of hepatic glutamine synthetase. *Hepatology* **2005,** *42* (2), 499-499.
6. Case, D. A.; Babin, V.; Berryman, J. T.; Betz, R. M.; Cai, Q.; Cerutti, D. S.; Cheatham III, T. E.; Darden, T. A.; Duke, R. E.; Gohlke, H.; Goetz, A. W.; Gusarov, S.; Homeyer, N.; Janowski, P.; Kaus, J.; Kolossváry, I.; Kovalenko, A.; Lee, T. S.; LeGrand, S.; Luchko, T.; Luo, R.; Madej, B.; Merz, K. M.; Paesani, F.; Roe, D. R.; Roitberg, A.; Sagui, C.; Salomon-Ferrer, R.; Seabra, G.; Simmerling, C. L.; Smith, W.; Swails, J.; Walker, R. C.; Wang, J.; Wolf, R. M.; Wu, X.; Kollman, P. A., AMBER 14. *University of California, San Francisco.* **2014**.
7. Case, D. A.; Betz, R. M.; Botello-Smith, W.; Cerutti, D. S.; Cheatham III, T. E.; Darden, T. A.; Duke, R. E.; Giese, T. J.; Gohlke, H.; Goetz, A. W.; Homeyer, N.; Izadi, S.; Janowski, P.; Kaus, J.; Kovalenko, A.; Lee, T. S.; LeGrand, S.; Li, P.; Lin, C.; Luchko, T.; Luo, R.; Madej, B.; Mermelstein, D.; Merz, K. M.; Monard, G.; Nguyen, H.; Nguyen, H. T.; Omelyan, I.; Onufriev, A.; Roe, D. R.; Roitberg, A.; Sagui, C.; Simmerling, C. L.; Swails, J.; Walker, R. C.; Wang, J.; Wolf, R. M.; Wu, X.; Xiao, L.; York, D. M.; Kollman, P. A., AMBER 16. *University of California, San Francisco.* **2016**.
8. Frieg, B.; Görg, B.; Homeyer, N.; Keitel, V.; Häussinger, D.; Gohlke, H., Molecular mechanisms of glutamine synthetase mutations that lead to clinically relevant pathologies. *PLoS Comput. Biol.* **2016,** *12* (2), e1004693.
9. Cornell, W. D.; Cieplak, P.; Bayly, C. I.; Gould, I. R.; Merz, K. M.; Ferguson, D. M.; Spellmeyer, D. C.; Fox, T.; Caldwell, J. W.; Kollman, P. A., A second generation force field for the simulation of proteins, nucleic acids, and organic molecules. *J. Am. Chem. Soc.* **1995,** *117* (19), 5179–5197.
10. Hornak, V.; Abel, R.; Okur, A.; Strockbine, B.; Roitberg, A.; Simmerling, C., Comparison of multiple Amber force fields and development of improved protein backbone parameters. *Proteins: Struct., Funct., Bioinf.* **2006,** *65* (3), 712-725.
11. Jorgensen, W. L.; Chandrasekhar, J.; Madura, J. D.; Impey, R. W.; Klein, M. L., Comparison of simple potential functions for simulating liquid water. *J. Chem. Phys.* **1983,** *79* (2), 926-935.
12. Bayly, C. I.; Cieplak, P.; Cornell, W. D.; Kollman, P. A., A well-behaved electrostatic potential based method using charge restraints for deriving atomic charges - the RESP Model. *J. Phys. Chem.* **1993,** *97* (40), 10269-10280.
13. Cornell, W. D.; Cieplak, P.; Bayly, C. I.; Kollman, P. A., Application of RESP charges to calculate conformational cnergies, hydrogen bond energies, and free-energies of solvation. *J. Am. Chem. Soc.* **1993,** *115* (21), 9620-9631.
14. Myung, Y.; Han, S., Force field parameters for 3-nitrotyrosine and 6-nitrotryptophan. *Bull. Korean Chem. Soc.* **2010,** *31* (9), 2581-2587.
15. Meagher, K. L.; Redman, L. T.; Carlson, H. A., Development of polyphosphate parameters for use with the AMBER force field. *J. Comput. Chem.* **2003,** *24* (9), 1016-1025.
16. Allner, O.; Nilsson, L.; Villa, A., Magnesium ion-water coordination and exchange in biomolecular simulations. *J. Chem. Theory Comput.* **2012,** *8* (4), 1493-1502.
17. Salomon-Ferrer, R.; Götz, A. W.; Poole, D.; Le Grand, S.; Walker, R. C., Routine microsecond molecular dynamics simulations with Amber on GPUs. 2. Explicit solvent particle mesh Ewald. *J. Chem. Theory Comput.* **2013,** *9* (9), 3878-3888.
18. Galindo-Murillo, R.; Roe, D. R.; Cheatham III, T. E., Convergence and reproducibility in molecular dynamics simulations of the DNA duplex d(GCACGAACGAACGAACGC). *Biochim. Biophys. Acta.* **2015,** *1850* (5), 1041-58.
19. Roe, D. R.; Cheatham III, T. E., PTRAJ and CPPTRAJ: software for processing and analysis of molecular dynamics trajectory data. *J. Chem. Theory Comput.* **2013,** *9* (7), 3084-3095.
20. Gohlke, H.; Case, D. A., Converging free energy estimates: MM-PB(GB)SA studies on the protein-protein complex Ras-Raf. *J. Comput. Chem.* **2004,** *25* (2), 238-250.

21. Homeyer, N.; Stoll, F.; Hillisch, A.; Gohlke, H., Binding free energy calculations for lead optimization: Assessment of their accuracy in an industrial drug design context. *J. Chem. Theory Comput.* **2014,** *10*, 3331–3344.
22. Homeyer, N.; Gohlke, H., Free energy calculations by the molecular mechanics Poisson-Boltzmann surface area method. *Mol. Inf.* **2012,** *31* (2), 114-122.
23. Srinivasan, J.; Cheatham, I., T. E.; Cieplak, P.; Kollman, P. A.; Case, D. A., Continuum solvent studies of the stability of DNA, RNA, and phosphoramidate - DNA helices. *J. Am. Chem. Soc.* **1998,** *120* (37), 9401-9409.
24. Case, D. A.; Darden, T. A.; Cheatham III, T. E.; Simmerling, C. L.; Wang, J.; Duke, R. E.; Luo, R.; Walker, R. C.; Zhang, W.; Merz, K. M.; Roberts, B.; Hayik, S.; Roitberg, A.; Seabra, G.; Swails, J.; Götz, A. W.; Kolossváry, I.; Wong, K. F.; Paesani, F.; Vanicek, J.; Wolf, R. M.; Liu, J.; Wu, X.; Brozell, S. R.; Steinbrecher, T.; Gohlke, H.; Cai, Q.; Ye, X.; Wang, J.; Hsieh, M.-J.; Cui , G.; Roe, D. R.; Mathews, D. H.; Seetin, M. G.; Salomon-Ferrer, R.; Sagui, C.; Babin, V.; Luchko, T.; Gusarov, S.; Kovalenko, A.; Kollman, P. A., AMBER 12. *University of California, San Francisco.* **2012**.
25. Hou, T.; Wang, J.; Li, Y.; Wang, W., Assessing the performance of the MM/PBSA and MM/GBSA methods. 1. The accuracy of binding free energy calculations based on molecular dynamics simulations. *J. Chem. Inf. Model.* **2011,** *51* (1), 69-82.
26. Mobley, D. L.; Gilson, M. K., Predicting binding free energies: frontiers and benchmarks. *Annu. Rev. Biophys.* **2017,** *46*, 531-558.
27. Aleksandrov, A.; Thompson, D.; Simonson, T., Alchemical free energy simulations for biological complexes: powerful but temperamental... *J Mol Recognit* **2010,** *23* (2), 117-127.
28. Chodera, J. D.; Mobley, D. L.; Shirts, M. R.; Dixon, R. W.; Branson, K.; Pande, V. S., Alchemical free energy methods for drug discovery: progress and challenges. *Curr Opin Struct Biol* **2011,** *21* (2), 150-160.
29. Jorgensen, W. L.; Thomas, L. L., Perspective on free-energy perturbation calculations for chemical equilibria. *J. Chem. Theory Comput.* **2008,** *4* (6), 869-876.
30. Bhati, A. P.; Wan, S. Z.; Wright, D. W.; Coveney, P. V., Rapid, accurate, precise, and reliable relative free energy prediction using ensemble based thermodynamic integration. *J. Chem. Theory Comput.* **2017,** *13* (1), 210-222.
31. Steinbrecher, T.; Joung, I.; Case, D. A., Soft-core potentials in thermodynamic integration: comparing one- and two-step transformations. *J. Comput. Chem.* **2011,** *32* (15), 3253-63.
32. Michel, J.; Essex, J. W., Prediction of protein-ligand binding affinity by free energy simulations: assumptions, pitfalls and expectations. *J. Comput.-Aided. Mol. Des.* **2010,** *24* (8), 639-658.
33. Darden, T.; Pearlman, D.; Pedersen, L. G., Ionic charging free energies: spherical versus periodic boundary conditions. *J. Chem. Phys.* **1998,** *109* (24), 10921-10935.
34. Loccisano, A. E.; Acevedo, O.; DeChancie, J.; Schulze, B. G.; Evanseck, J. D., Enhanced sampling by multiple molecular dynamics trajectories: carbonmonoxy myoglobin 10 mu s A0 -> A(1-3) transition from ten 400 picosecond simulations. *J Mol Graph Model* **2004,** *22* (5), 369-376.
35. Likic, V. A.; Gooley, P. R.; Speed, T. P.; Strehler, E. E., A statistical approach to the interpretation of molecular dynamics simulations of calmodulin equilibrium dynamics. *Protein Sci* **2005,** *14* (12), 2955-2963.
36. Chipot, C.; Pohorille, A., Calculating free energy differences using perturbation theory. In *Free energy calculations*, Chipot, C.; Pohorille, A., Eds. 2007; pp 33-75.
37. Cournia, Z.; Allen, B.; Sherman, W., Relative binding free energy calculations in drug discovery: recent advances and practical considerations. *J. Chem. Inf. Model.* **2017,** *57* (12), 2911-2937.
38. Case, D. A.; Ben-Shalom, I. Y.; Brozell, S. R.; Cerutti, D. S.; Cheatham, I., T.E.; Cruzeiro, V. W. D.; Darden, T. A.; Duke, R. E.; Ghoreishi, D.; Gilson, M. K.; Gohlke, H.; Goetz, A. W.; Greene, D.; Harris, R.; Homeyer, N.; Izadi, S.; Kovalenko, A.; Kurtzman, T.; Lee, T. S.; LeGrand, S.; Li, P.; Lin, C.; Liu, J.; Luchko, T.; Luo, R.; Mermelstein, D. J.; Merz, K. M.; Miao, Y.; Monard, G.; Nguyen, C.; Nguyen, H.; Omelyan, I.; Onufriev, A.; Pan, F.; Qi, R.; Roe, D. R.; Roitberg, A.; Sagui, C.; Schott-Verdugo, S.; Shen, J.; Simmerling, C. L.; Smith, J.; Salomon-Ferrer, R.; Swails, J.; Walker, R. C.; Wang, J.; Wei, H.; Wolf, R. M.; Wu, X.; Xiao, L.; York, D. M.; Kollman, P. A., AMBER 18. *University of California, San Francisco.* **2018**.
39. Lee, T. S.; Hu, Y.; Sherborne, B.; Guo, Z.; York, D. M., Toward fast and accurate binding affinity prediction with pmemdGTI: an efficient implementation of GPU-accelerated thermodynamic integration. *J. Chem. Theory Comput.* **2017,** *13* (7), 3077-3084.
40. Mermelstein, D. J.; Lin, C.; Nelson, G.; Kretsch, R.; McCammon, J. A.; Walker, R. C., Fast and flexible gpu accelerated binding free energy calculations within the amber molecular dynamics package. *J. Comput. Chem.* **2018,** *39* (19), 1354-1358.
41. Kottalam, J.; Case, D. A., Dynamics of ligand escape from the heme pocket of myoglobin. *J. Am. Chem. Soc.* **1988,** *110* (23), 7690-7697.

42. Kumar, S.; Bouzida, D.; Swendsen, R. H.; Kollman, P. A.; Rosenberg, J. M., The weighted histogram analysis method for free-energy calculations on biomolecules. 1. The method. *J. Comput. Chem.* **1992,** *13* (8), 1011-1021.
43. Simonson, T.; Carlsson, J.; Case, D. A., Proton binding to proteins: pK(a) calculations with explicit and implicit solvent models. *J. Am. Chem. Soc.* **2004,** *126* (13), 4167-4180.
44. Team, R. C., TEAM: R: a language and environment for statistical computing. *R Foundation for Statistical Computing, Vienna, Austria* **2008**.
45. Listrom, C. D.; Morizono, H.; Rajagopal, B. S.; McCann, M. T.; Tuchman, M.; Allewell, N. M., Expression, purification, and characterization of recombinant human glutamine synthetase. *Biochem. J.* **1997,** *328*, 159-163.
46. Jeitner, T. M.; Cooper, A. J. L., Inhibition of human glutamine synthetase by L-methionine-S, R-sulfoximine-relevance to the treatment of neurological diseases. *Metab. Brain Dis.* **2014,** *29* (4), 983-989.
47. Görg, B.; Qvartskhava, N.; Voss, P.; Grune, T.; Häussinger, D.; Schliess, F., Reversible inhibition of mammalian glutamine synthetase by tyrosine nitration. *FEBS Lett.* **2007,** *581* (1), 84-90.
48. Kingdon, H. S.; Hubbard, J. S.; Stadtman, E. R., Regulation of glutamine synthetase. XI. The nature and implications of a lag phase in the Escherichia coli glutamine synthetase reaction. *Biochemistry* **1968,** *7* (6), 2136-2142.
49. Moreira, C.; Ramos, M. J.; Fernandes, P. A., Glutamine synthetase drugability beyond its active site: exploring oligomerization interfaces and pockets. *Molecules* **2016,** *21* (8).
50. Lindorff-Larsen, K.; Piana, S.; Palmo, K.; Maragakis, P.; Klepeis, J. L.; Dror, R. O.; Shaw, D. E., Improved side-chain torsion potentials for the Amber ff99SB protein force field. *Proteins: Struct., Funct., Bioinf.* **2010,** *78* (8), 1950-1958.
51. Maier, J. A.; Martinez, C.; Kasavajhala, K.; Wickstrom, L.; Hauser, K. E.; Simmerling, C., ff14SB: Improving the accuracy of protein side chain and backbone parameters from ff99SB. *J. Chem. Theory Comput.* **2015,** *11* (8), 3696-3713.
52. Riniker, S., Fixed-charge atomistic force fields for molecular dynamics simulations in the condensed phase: An overview. *J. Chem. Inf. Model.* **2018,** *58* (3), 565-578.
53. Galindo-Murillo, R.; Robertson, J. C.; Zgarbova, M.; Sponer, J.; Otyepka, M.; Jurecka, P.; Cheatham III, T. E., Assessing the current state of Amber force field modifications for DNA. *J. Chem. Theory Comput.* **2016,** *12* (8), 4114-4127.
54. Hobza, P.; Sponer, J., Structure, energetics, and dynamics of the nucleic acid base pairs: Nonempirical ab initio calculations. *Chem. Rev.* **1999,** *99* (11), 3247-3276.
55. Sponer, J.; Riley, K. E.; Hobza, P., Nature and magnitude of aromatic stacking of nucleic acid bases. *Phys. Chem. Chem. Phys.* **2008,** *10* (19), 2595-2610.
56. Sponer, J.; Sponer, J. E.; Mladek, A.; Jurecka, P.; Banas, P.; Otyepka, M., Nature and magnitude of aromatic base stacking in DNA and RNA: Quantum chemistry, molecular Mechanics, and experiment. *Biopolymers* **2013,** *99* (12), 978-988.
57. Parker, T. M.; Sherrill, C. D., Assessment of empirical models versus high-accuracy ab initio methods for nucleobase stacking: evaluating the importance of charge penetration. *J. Chem. Theory Comput.* **2015,** *11* (9), 4197-204.
58. Dror, R. O.; Dirks, R. M.; Grossman, J. P.; Xu, H. F.; Shaw, D. E., Biomolecular simulation: a computational microscope for molecular biology. *Annu. Rev. Biophys.* **2012,** *41*, 429-452.
59. Caves, L. S. D.; Evanseck, J. D.; Karplus, M., Locally accessible conformations of proteins: Multiple molecular dynamics simulations of crambin. *Protein Sci* **1998,** *7* (3), 649-666.
60. Buch, I.; Giorgino, T.; De Fabritiis, G., Complete reconstruction of an enzyme-inhibitor binding process by molecular dynamics simulations. *Proc. Natl. Acad. Sci. U. S. A.* **2011,** *108* (25), 10184-10189.
61. Ryckaert, J. P.; Ciccotti, G.; Berendsen, H. J. C., Numerical integration of cartesian equations of motion of a system with constraints molecular dynamics of n-alkanes. *J. Comput. Phys.* **1977,** *23* (3), 327-341.
62. Genheden, S.; Ryde, U., The MM/PBSA and MM/GBSA methods to estimate ligand-binding affinities. *Expert. Opin. Drug. Dis.* **2015,** *10* (5), 449-461.
63. Lepsik, M.; Kriz, Z.; Havlas, Z., Efficiency of a second-generation HIV-1 protease inhibitor studied by molecular dynamics and absolute binding free energy calculations. *Proteins: Struct., Funct., Genet.* **2004,** *57* (2), 279-293.
64. Spackova, N.; Cheatham III, T. E.; Ryjacek, F.; Lankas, F.; van Meervelt, L.; Hobza, P.; Sponer, J., Molecular dynamics simulations and thermodynamics analysis of DNA-drug complexes. Minor groove binding between 4 ',6-diamidino-2-phenylindole and DNA duplexes in solution. *J. Am. Chem. Soc.* **2003,** *125* (7), 1759-1769.
65. Gilson, M. K.; Zhou, H. X., Calculation of protein-ligand binding affinities. *Annu Rev Biophys Biomol Struct* **2007,** *36*, 21-42.
66. Weis, A.; Katebzadeh, K.; Soderhjelm, P.; Nilsson, I.; Ryde, U., Ligand affinities predicted with the MM/PBSA method: dependence on the simulation method and the force field. *J. Med. Chem.* **2006,** *49* (22), 6596-606.

67. Wan, S. Z.; Knapp, B.; Wright, D. W.; Deane, C. M.; Coveney, P. V., Rapid, precise, and reproducible prediction of peptide-MHC binding affinities from molecular dynamics that correlate well with experiment. *J. Chem. Theory Comput.* **2015,** *11* (7), 3346-3356.
68. Wright, D. W.; Hall, B. A.; Kenway, O. A.; Jha, S.; Coveney, P. V., Computing clinically relevant binding free energies of HIV-1 protease inhibitors. *J. Chem. Theory Comput.* **2014,** *10* (3), 1228-1241.
69. Genheden, S.; Ryde, U., How to obtain statistically converged MM/GBSA results. *J. Comput. Chem.* **2010,** *31* (4), 837-846.
70. Sitkoff, D.; Sharp, K. A.; Honig, B., Accurate calculation of hydration free-energies using macroscopic solvent models. *J. Phys. Chem.* **1994,** *98* (7), 1978-1988.
71. Hou, T.; Wang, J. M.; Li, Y. Y.; Wang, W., Assessing the performance of the molecular mechanics/Poisson Boltzmann surface area and molecular mechanics/generalized Born surface area methods. II. The accuracy of ranking poses generated from docking. *J. Comput. Chem.* **2011,** *32* (5), 866-877.
72. Sun, H. Y.; Li, Y. Y.; Shen, M. Y.; Tian, S.; Xu, L.; Pan, P. C.; Guan, Y.; Hou, T. J., Assessing the performance of MM/PBSA and MM/GBSA methods. 5. Improved docking performance using high solute dielectric constant MM/GBSA and MM/PBSA rescoring. *Phys. Chem. Chem. Phys.* **2014,** *16* (40), 22035-22045.
73. Steinbrecher, T.; Case, D. A.; Labahn, A., A multistep approach to structure-based drug design: studying ligand binding at the human neutrophil elastase. *J. Med. Chem.* **2006,** *49* (6), 1837-1844.
74. Persch, E.; Dumele, O.; Diederich, F., Molecular recognition in chemical and biological systems. *Angew. Chem. Int. Edit.* **2015,** *54* (11), 3290-3327.
75. Coveney, P. V.; Wan, S. Z., On the calculation of equilibrium thermodynamic properties from molecular dynamics. *Phys. Chem. Chem. Phys.* **2016,** *18* (44), 30236-30240.
76. Wan, S. Z.; Coveney, P. V., Rapid and accurate ranking of binding affinities of epidermal growth factor receptor sequences with selected lung cancer drugs. *J Royal Soc Interface* **2011,** *8* (61), 1114-1127.
77. Plattner, N.; Noé, F., Protein conformational plasticity and complex ligand-binding kinetics explored by atomistic simulations and Markov models. *Nat. Commun.* **2015,** *6*.
78. Koller, A. N.; Bozilovic, J.; Engels, J. W.; Gohlke, H., Aromatic N versus aromatic F: bioisosterism discovered in RNA base pairing interactions leads to a novel class of universal base analogs. *Nucleic Acids Res* **2010,** *38* (9), 3133-3146.
79. Ciupka, D.; Gohlke, H., On the potential alternate binding change mechanism in a dimeric structure of Pyruvate Phosphate Dikinase. *Sci Rep-Uk* **2017,** *7*.
80. Minges, A.; Ciupka, D.; Winkler, C.; Hoppner, A.; Gohlke, H.; Groth, G., Structural intermediates and directionality of the swiveling motion of Pyruvate Phosphate Dikinase. *Sci Rep-Uk* **2017,** *7*.
81. Bastug, T.; Chen, P. C.; Patra, S. M.; Kuyucak, S., Potential of mean force calculations of ligand binding to ion channels from Jarzynski's equality and umbrella sampling. *J. Chem. Phys.* **2008,** *128* (15).
82. Kästner, J., Umbrella sampling. *Wires Comput Mol Sci* **2011,** *1* (6), 932-942.